Akademia Górniczo-Hutnicza im. Stanisława Staszica w Krakowie
WYDZIAŁ FIZYKI I INFORMATYKI STOSOWANEJ

KATEDRA ODDZIAŁYWAŃ I DETEKCJI CZĄSTEK

Projekt dyplomowy

Measurement of muon trigger efficiency using the Tag and Probe method in ultra-peripheral heavy-ion collisions of lead-lead at 5.36 TeV in the ATLAS experiment at the LHC

Pomiar wydajności trygera mionowego przy użyciu metody Tag and Probe w zderzeniach ultraperyferycznych ciężkich jonów ołowiu z ołowiem przy energii 5,36 TeV w eksperymencie ATLAS w LHC

Autor: Szymon Mateusz Cisek
Kierunek: Fizyka Techniczna
Opiekun pracy: prof. dr hab. inż. Iwona Grabowska-Bołd

Kraków, 2026

Contents

1 Introduction

Researching the basic properties of elementary particles and studying their interactions are some of the methods used to explore the fundamental laws of physics that exist in the Universe. The Large Hadron Collider (LHC) at the European Organization for Nuclear Research (CERN), located near the Swiss-French border, provides a perfect environment for analysing and achieving a deeper understanding of particle physics.

The LHC is the world's largest particle accelerator, with a circumference of 27 kilometres and located 175 meters underground. The centre-of-mass energy, denoted as $\sqrt{s}$, in Run 3 (2022-2025) for proton-proton (pp) collisions, reached a world record energy for particle accelerators of $\sqrt{s} = 13.6$ TeV (6.8 TeV per beam). This thesis focuses on heavy-ion collisions also provided at the LHC with beams of lead (Pb) ions accelerated to 99.999993% of the speed of light with an energy of $\sqrt{s_{\mathrm{NN}}} = 5.36$ TeV per nucleon pair.

The ultra-relativistic Pb beams are sources of high-intensity electromagnetic fields that can be interpreted as quasi-real photon fluxes scaling with the square of the nuclear charge Z^2 per nucleus. Ultra-peripheral collisions (UPC) occur when two of the nuclei do not overlap with each other. It yields a clean environment for studying photon-photon ($\gamma\gamma$) interactions. The subject of interest in this work is the $\gamma\gamma \to \mu^+\mu^-$ (dimuon) process, which is used to measure the muon trigger efficiency. The proton/ion collision rate delivered to the ATLAS detector is extremely high; it is impossible to save all the data. Therefore, the two-stage trigger system (Level-1 and High Level Trigger) is employed to select and store only the interesting events.

The dataset comes from 2023, with the total integrated luminosity $L_{int} = 1.63\,\mathrm{nb}^{-1}$. The $\gamma\gamma \to \mu^+\mu^-$ signal process is generated by the SuperChic Monte Carlo (MC) generator, interfaced with Pythia8, which simulates the final-state radiation. The MC sample is divided into three groups by the mass of the muon pair: 4-7 GeV (4M7), 7-20 GeV (7M20), and above 20 GeV (20M).

The dedicated event selection to obtain a clean sample of the $\gamma\gamma \to \mu^+\mu^-$ signal is applied to the 2023 dataset and is described in detail in Section 3.2. To measure the trigger efficiency, the tag-and-probe method is employed for the data, and MC simulation; the tag muon must satisfy tight offline requirements, while the probe muon is required to be an unbiased object. The tag and probe muons are expected to originate from the $\gamma\gamma \to \mu^+\mu^-$ process. The trigger efficiency is defined as the ratio of the probes that satisfy the trigger matching criteria to the total number of probes.

The Level-1 trigger efficiencies for the data and the MC simulation are presented as p_T-$q\eta$ efficiency maps, along with the 1D projections in 11 $q\eta$ (charge-signed pseudorapidity) intervals (see Section 2.6 for definitions of p_T and η). The scale factors (SFs) are defined as the ratio of the Level-1 trigger efficiencies measured in data to those obtained in the MC simulation. In the physics analyses, the SFs are applied to correct the MC simulation in case differences between trigger efficiencies in data and simulation are measured. The resulting SFs are close to unity in the endcap regions, but in the barrel region, they tend to be lower by up to about 20% relative to unity.

The (asymmetric) statistical uncertainties on the efficiencies are computed using the Clopper-Pearson method. Since this procedure yields asymmetric confidence intervals, the upper and lower uncertainties are propagated to the SFs separately. In addition, the systematic uncertainties are assessed by considering several sources, which are described in detail in Section 5.2.

The final part of this thesis presents a preliminary analysis of the early 2025 Pb+Pb data collected at $\sqrt{s_{\mathrm{NN}}} = 5.36$ TeV with an integrated luminosity of $0.9841\,\mathrm{nb}^{-1}$, together with a comparison to the reference 2023 data. The Author of the thesis assisted at heavy-ion data taking in November 2025 at CERN. The same event selection is applied to both datasets, and the Level-1 trigger efficiencies are measured using the tag-and-probe method.

2 ATLAS experiment and detector

ATLAS (A Toroidal LHC Apparatus) is the largest general-purpose experiment at the LHC, aiming to expand our knowledge of elementary particles and their interactions. To this end, ATLAS mainly studies pp, Pb+Pb, and p+Pb collisions, the products of which are recorded by the ATLAS detector. The project's main achievements include the discovery of the Higgs boson [1], observation of light-by-light scattering [2], and the production of the Higgs boson in association with top quarks (ttH) [3].

2.1 The ATLAS detector

The ATLAS detector [4] is one of the world's largest particle detectors. It is cylindrical in shape, measuring about 46 m in length and 25 m in diameter, with a mass of approximately 7000 tons. As a detector, ATLAS was conceived for general-purposes; thus, it is optimised to measure a broad spectrum of signals rather than specific physical processes. The primary systems of the detector are the Inner Detector, the Electromagnetic and Hadronic Calorimeters, the Muon Spectrometer, and the Superconducting Magnet System. A multi-level trigger and data acquisition system is employed to select and record the most significant collision events.

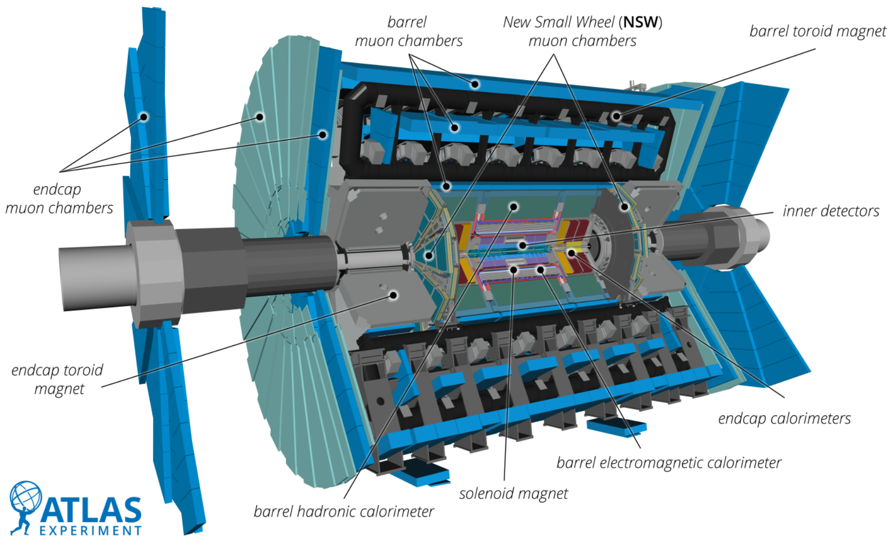

Figure 1: ATLAS detector schematic for Run 3 [4]

2.2 The Inner Detector

The Inner Detector (ID) [5] is divided into three main components: the Pixel Detector, the Semiconductor Tracker (SCT), and the Transition Radiation Tracker (TRT). The superconducting solenoid surrounds the entire ID and generates a 2 T magnetic field parallel to the beam axis. This field bends the trajectories of the charged particles, enabling measurements of their kinematic variables.

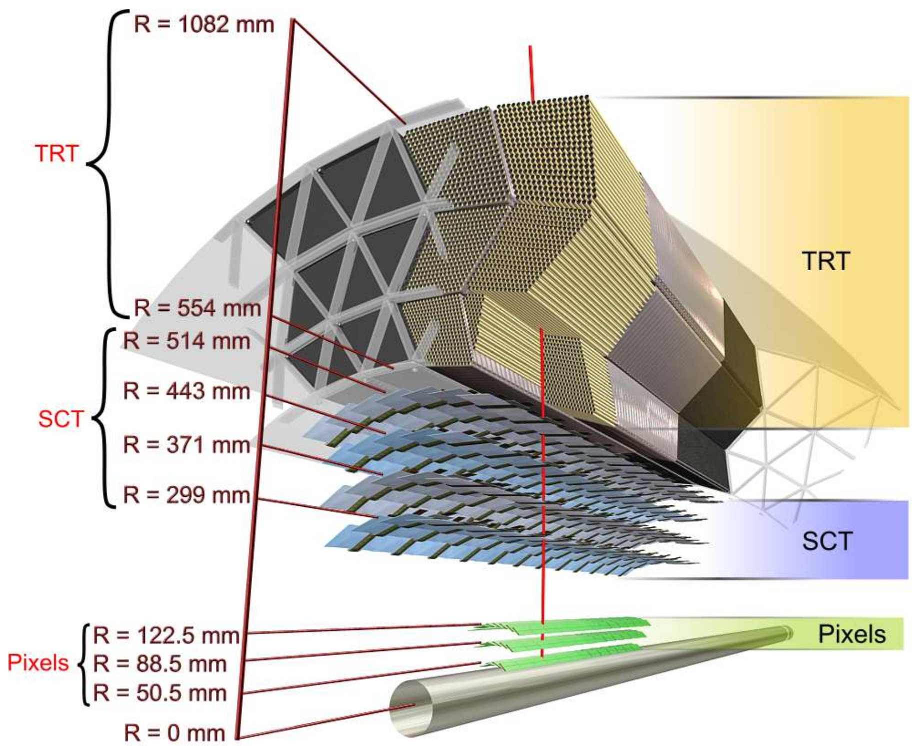

Figure 2: The Inner Detector structure [5]

The Pixel Detector is constructed from four layers of silicon pixels, which are the first to interact with decay products emerging from the interaction point, located near the beam axis at a radius of approximately 3.3 cm. Charged particles leave a trace in the form of a relatively small energy deposit; it helps to examine the position of the primary vertex of the specific event. The signal measurement precision is roughly 10 µm. The detector consists of 92 million pixels, and almost 2000 detector elements.

A relevant detector component that allows for the detection and reconstruction of particle tracks is the SCT. It comprises 4088 two-sided modules with about 6 million silicon micro-strip sensors and is configured so that each charged particle usually leaves hits in four layers.

The third and final tracking system is the TRT. In contrast to the other two layers, it consists of 300000 thin-walled drift tubes ("straws") with a diameter of 4 mm and a 30 µm gold-plated tungsten wire at their centre. Furthermore, in addition to track reconstruction, the TRT provides particle identification because each straw is filled with an Xe-based gas mixture. When charged particles pass through the gas, they ionise it and generate a detectable electrical signal.

2.3 Electromagnetic and Hadronic Calorimeters

The calorimeter system [6] in ATLAS measures particle energies with high precision, particularly for photons, electrons, and hadrons, and it supports particle identification. It is a sampling structure in which highly dense absorber layers develop electromagnetic or hadronic "showers" interleaved with active gaps that record the deposited energy.

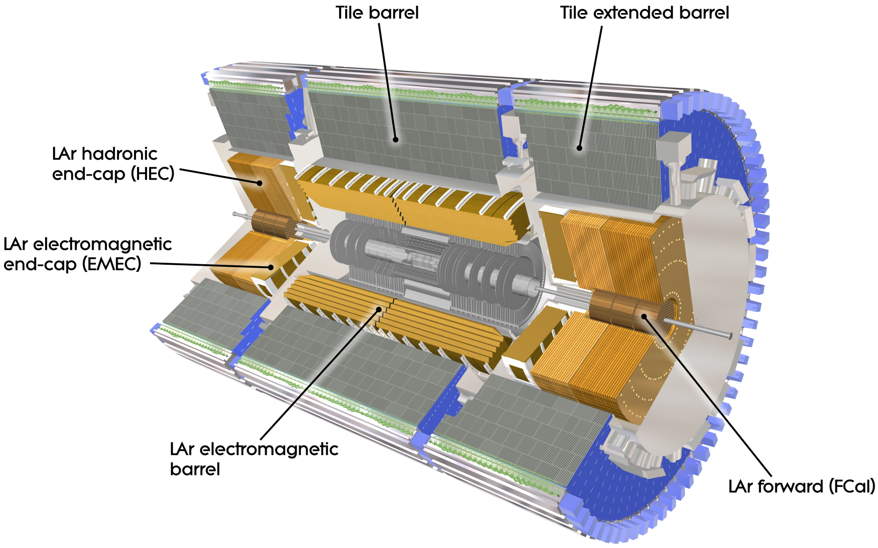

Figure 3: The calorimeter system in ATLAS [6]

The Inner Detector is surrounded by the Liquid Argon (LAr) Calorimeter, which measures the energies of electrons and photons. Layers of metals, primarily lead, copper, or tungsten, are responsible for absorbing particles and, as a result, generating electromagnetic showers via bremsstrahlung and pair production. New lower energy particles that stem from the showers ionise liquid argon at a temperature of −184 °C, which is sandwiched between the layers, and then provide an electrical signal that is shaped and digitised by front-end electronics. In the central region of the calorimeter, electrons and photons are measured; the geometry in this area has a characteristic accordion structure with a honeycomb pattern. The LAr endcap comprises the forward calorimeter (FCal), electromagnetic endcap (EMEC), and hadronic endcap (HEC). Electromagnetic endcaps each have a thickness of 0.632 m and a radius of 2.077 m; hadronic endcaps are built from two wheel-like disks with thicknesses of 0.8 m and 1.0 m and a radius of 2.09 m. The FCal consists of three modules with a radius of 0.455 m and a thickness of 0.45 m each.

The Tile Calorimeter sits outside the LAr electromagnetic calorimeter and is designed to measure the energy of hadronic particles, whose energy is not fully deposited. By analogy to the LAr electromagnetic calorimeter, the principle of operation is similar; the absorber is made of steel, and instead of liquid argon, plastic scintillation tiles are used to produce photons that are transformed into an electric current, which is proportional to the original particle's energy. The total weight of the Tile Calorimeter is about 2900 tons (the heaviest part of the ATLAS detector), the central barrel is made of 64 azimuthal sectors, each 5.6 m long. The two extended barrels have 64 modules, each 2.6 m in length.

2.4 Muon Spectrometer

Muons and electrons are similar particles, both are classified as leptons. However, muons are heavier than electrons and have a mass of 105.66 MeV/c^2 (105.66 MeV in natural units $c = \hbar = 1$). The calorimeter system is not capable of detecting incoming muons from the interaction point (IP) because muons at typical LHC energies behave as minimum-ionizing particles: they emit far less bremsstrahlung, so they traverse the calorimeters with limited energy deposition. For this reason, the Muon Spectrometer (MS) [7] is required to detect muons and measure their momenta. Five different detection system mechanisms are used: Thin Gap Chambers, Resistive Plate Chambers, Monitored Drift Tubes, Small-Strip Thin-Gap Chambers, and Micromegas.

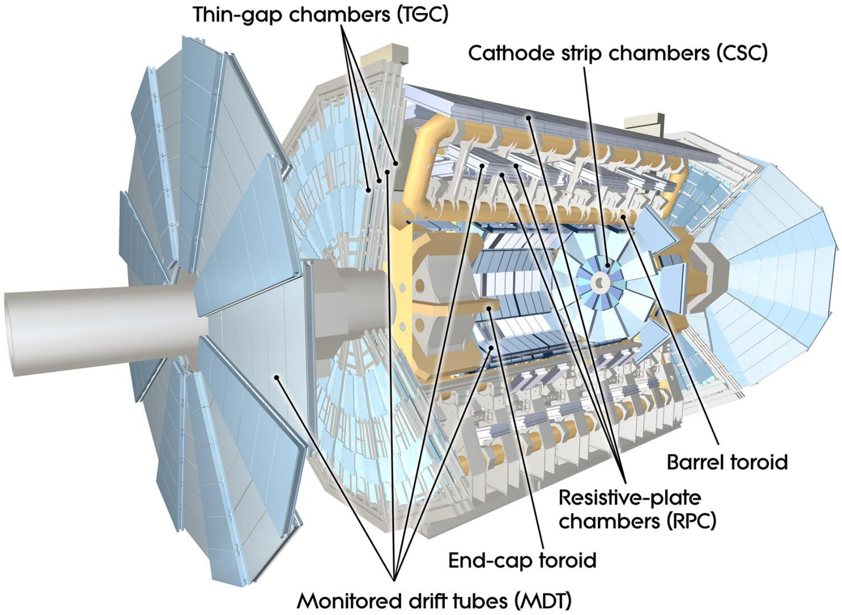

Figure 4: The Muon Spectrometer in ATLAS [7]

The Monitored Drift Tubes (MDT) are used as precision detectors to measure the position of muons with a spatial resolution of a 80 µm. The MDTs are constructed from aluminium tubes with a diameter of 3 cm filled with an Ar-based gas mixture. As muons traverse the detector, electrons are ejected and drift towards a wire at the centre of the tube, releasing an electric signal. In general, there are 1171 chambers with a total of 354240 tubes, length of the MDTs is in the range of 0.85 m to 6.5 m.

The Resistive Plate Chambers (RPCs) provide coverage in the central region of the ATLAS detector; each chamber consists of two highly resistive bakelite electrodes at an electric potential difference, and the volume between them is filled with a gas mixture. The Thin Gap Chambers (TGCs) are installed in the endcap region of the detector and comprise parallel 50 µm wires in a gas mixture. These two detectors are primarily used for the fast trigger system and also serve as a preliminary system for track reconstruction. The RPCs consist of 380,000 channels and have an electric field of 5000 V/mm. The TGCs, on the other hand, have 440,000 channels.

The Small-Strip Thin-Gap Chambers (sTGC) are additional detectors that consist of a grid of gold-plated tungsten wires with a diameter of 50 µm and a strip pitch of 3.2 mm. The operating principle is analogous to that of the TGC, but the sTGC technology is specifically designed for high-intensity LHC collisions.

The Small Wheel (SW) detector was replaced by the New Small Wheel (NSW) [8] to reduce the fake muon rate in the Level-1 trigger system; it uses sTGC and Micromegas (MM) technology. The Micromegas (MM) is a gaseous detector filled with Ar:CO_2 (93:7) in the Drift/conversion gap of 5 mm and a thin amplification gap of 128 µm, separated by a metallic mesh. In total, the NSW MM system comprises about 2.1 million readout strips, which ensure a high resolution of order 100 µm per layer for the tracking system of offline muons. The upgrade is crucial for the next stages of the experiment, where the collision rate will be much larger than in the past.

2.5 Superconducting Magnet System

The Magnet System [9] at ATLAS serves to bend charged particles in order to measure their momentum and determine the sign of the electric charge. Two types of superconducting magnets are used: solenoidal and toroidal. To maintain the superconductivity of the magnets, they are cooled to about 4.5 K (−268 °C).

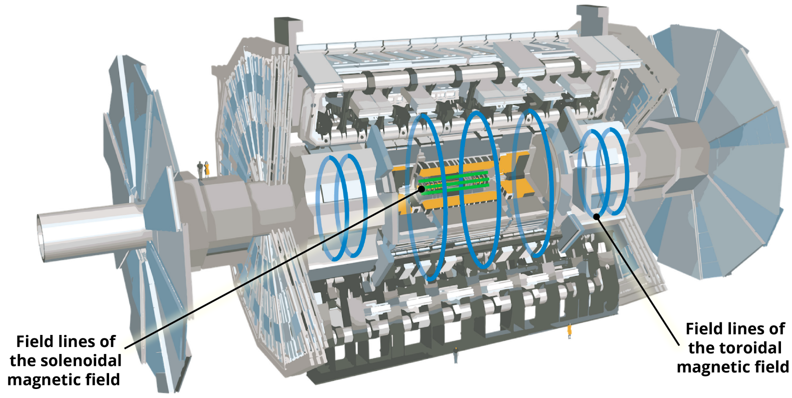

Figure 5: The ATLAS Magnet System [9]

The Central Solenoid Magnet surrounds the Inner Detector and provides a magnetic field of 2 T. It is 5.8 m long, 2.56 m in outer diameter, 4.5 cm thick, and weighs over 5 tons. This enormous magnetic field is obtained by using 9 km superconducting wire made of niobium-titanium, through which 7.73 kA of nominal current flows.

The barrel and end-cap toroid magnets are employed to measure the momentum of the muons by bending their tracks. The central toroid weighs about 830 tons, with a length of 25.3 m and an outer diameter of 20.1 m, making it the largest toroidal magnet ever built. It utilizes over 56 km of superconducting wire with 20.5 kA nominal current to generate a magnetic field of 3.5 T. The end-cap toroid is employed to extend the magnetic field for particles leaving the detector. Each end-cap magnet weighs about 240 tons, has 5 m of axial length, 10.7 m in outer diameter, and uses 13 km of Al/NbTi/Cu superconductive wire with 20.5 kA nominal current.

2.6 The ATLAS coordinate system and kinematic variables

The ATLAS detector uses a right-handed Cartesian coordinate system with the origin at the IP, illustrated in Figure 6. The z-axis is aligned with the beam direction, the x-axis points from the IP to the centre of the LHC ring, and the y-axis points upward.

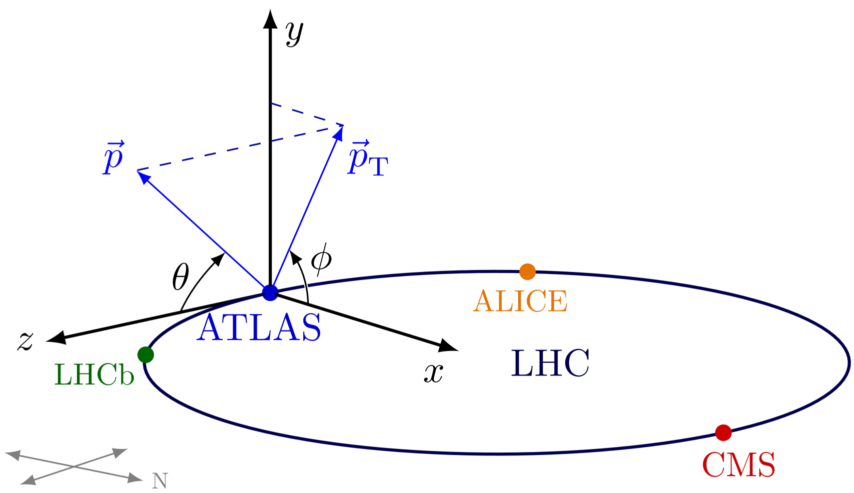

Figure 6: ATLAS conventional coordinate system with the LHC ring and other detectors [10]

The polar angle θ is measured from the positive z-axis, while the azimuthal angle ϕ is measured in the x-y plane from the positive x-axis towards the y-axis. The longitudinal "boost" along the z-axis in the pp occurs due to the different partonic Bjorken x scaling variables. On the other hand, boost in ultra-peripheral collisions of heavy-ions is a consequence of photon energy asymmetry. During the experiment, this boost is an unknown quantity, in practice, the three-momentum p is adopted less frequently than the transverse momentum p_T (Eq. 1).

$$p_T = |\mathbf{p}| \sin\theta \quad \text{or} \quad p_T = \sqrt{p_x^2 + p_y^2} \tag{1}$$

In experimental particle physics, rapidity and pseudorapidity variables are widely used to provide information about the angle relative to the beam axis. The rapidity of a particle is defined as

$$y = \frac{1}{2} \ln \frac{E + p_z}{E - p_z}, \tag{2}$$

where E is the measured energy. The usefulness of this variable stems from the additivity of rapidity under Lorentz's longitudinal boost. Particles that are moving perpendicular to the beam have $p_z = 0$; thus, $y = 0$.

The pseudorapidity is expressed exclusively in terms of the polar angle

$$\eta = -\ln \left[\tan\left(\frac{\theta}{2}\right) \right], \tag{3}$$

for ultra-relativistic (approximately massless) particles $\eta \simeq y$, Figure 7 illustrates the pseudorapidity regions with respect to the polar angle.

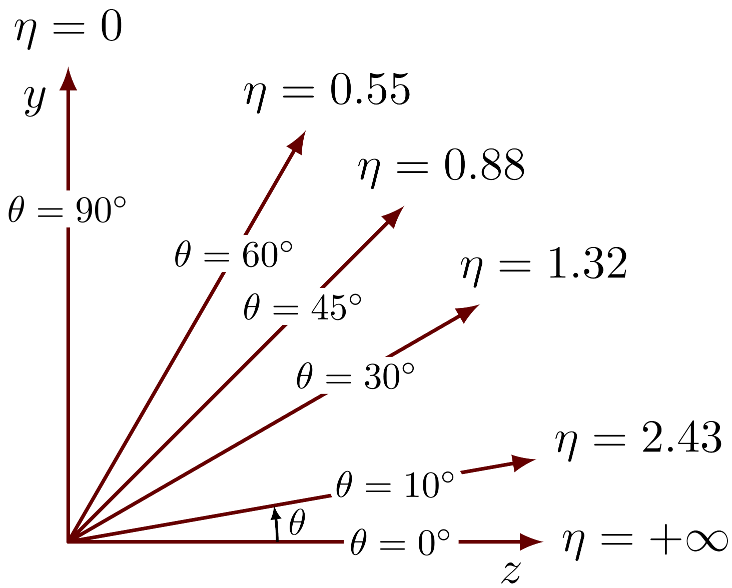

Figure 7: Pseudorapidity regions relative to the beam axis [11]

The invariant mass (m) of the decaying particle is a Lorentz-invariant quantity, and it can be reconstructed from the four-momenta of its decay products as

$$m = \sqrt{\left(\sum_{i=1}^{n} E_i\right)^2 - \left(\sum_{i=1}^{n} \mathbf{p}_i\right)^2}. \tag{4}$$

The angular distance between the two particles, denoted as ΔR, can be expressed in terms of η and ϕ

$$\Delta R = \sqrt{(\Delta\eta)^2 + (\Delta\phi)^2}. \tag{5}$$

Here, $\Delta\eta$ and $\Delta\phi$ represent the differences between the pseudorapidity and azimuthal angle of the two considered objects (leptons and jets), respectively. The ΔR metric provides a convenient measure for particle isolation criteria or matching criteria.

2.7 Dimuon production in UPC at the LHC

At the LHC, heavy-ion beams, such as lead (Pb) nuclei, are collided with each other for four weeks per year. The impact parameter (b), defined as the transverse distance between the centres of the two colliding nuclei, specifies the geometry and centrality of the event. For $b < 2R_A$, where R_A stands for a nuclear radius, the nuclei overlap with each other, producing a hot and dense quark-gluon plasma (QGP); $b \approx 0$ indicates a central collision, whereas $b \approx 2R_A$ is referred to as peripheral.

2.7.1 Equivalent Photon Approximation (EPA)

Strong electromagnetic (EM) fields generated by charged nuclei can produce configurations in which both nuclei do not overlap. So the impact parameter in the event is at least twice as large as the nuclear radius $b > 2R_A$. Such collisions are classified as "ultra-peripheral" (UPC), and in the Weizsäcker-Williams (W.W.) [12] [13] approach, known as the "equivalent photon approximation" (EPA), based on Fermi's proposal [14], the Lorentz-contracted EM field originating from the high-velocity nuclei can be interpreted as a quasi-real photon flux. When the wavelength of the photon is greater than the size of the nucleus, the nucleus acts as an effective source with charge Z - coherent production, where each photon flux scales with Z^2 per nucleus.

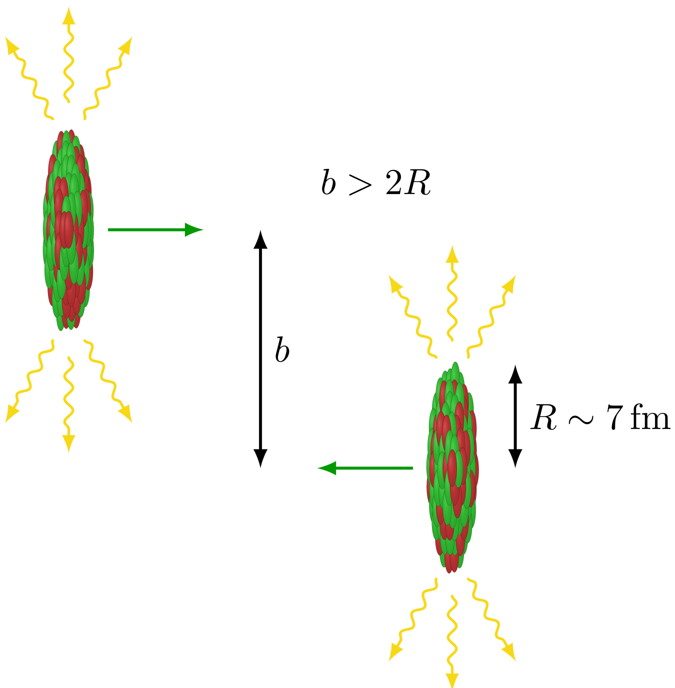

Figure 8: Illustration of Pb-Pb in UPC [15]

The cross section (σ_X) of the two-photon process, $\gamma\gamma \to X$, is defined as [16]

$$\sigma_X = \int d\omega_1 d\omega_2 \frac{n(\omega_1)}{\omega_1}\frac{n(\omega_2)}{\omega_2}\sigma_X^{\gamma\gamma}(\omega_1, \omega_2), \tag{6}$$

where $\sigma_X^{\gamma\gamma}$ is the cross section of the pure QED process of the $\gamma\gamma \to X$ leading to the X final state for incoming photons with energies $\omega_{1,2}$. The density of photon flux per unit area is denoted by $N(\omega, b)$, and it is used to obtain the energy spectrum of the ion $n(\omega)$ by

$$n(\omega) = \int N(\omega, b) d^2 b. \tag{7}$$

The Fourier's transform of the time dependent EM field of a moving charge results in

$$N(\omega, b) = \frac{Z^2 \alpha \omega^2}{\pi^2 \gamma_{rel}^2 \hbar^2 \beta^2 c^2} \left(K_1^2(x) + \frac{1}{\gamma^2} K_0^2(x) \right), \tag{8}$$

where Z is the ion charge, $\alpha \approx 1/137$ (fine-structure constant), $\gamma_{rel} = 2\gamma^2 - 1$ is the relative Lorentz factor of the particle, $\beta c = v$ is the velocity of the particle, and $K_{0,1}(x)$ are the modified Bessel functions, $x = \omega b / \gamma_{rel} \beta c \hbar$.

The modified Bessel functions $K_{0,1}(x)$ for $x \ll 1$ behave as $\sim -\ln x$ and $1/x$, respectively, whereas for $x \gg 1$, $K_{1,2}(x) \sim \sqrt{\frac{\pi}{2x}} e^{-x}$ [17]. The flux is strongly suppressed if $x \gg 1 \rightarrow \omega \gg \gamma_{rel} \hbar \beta c / b$; thus, the maximum energy of the photon (ω_{max}) can be approximated using the Heisenberg uncertainty principle formula

$$\omega_{max} \sim \frac{1}{\Delta t} \sim \frac{\gamma_{rel} \hbar v}{b}. \tag{9}$$

2.7.2 Experimental signatures of UPC dimuons

In the subsection above, the cross section in the EPA regime for the general process $\gamma\gamma \rightarrow X$ was written as a convolution of the photon flux $n(\omega)$ and the elementary cross section $\sigma_X^{\gamma\gamma}(\omega_1, \omega_2)$. In the specific case considered here, $X = \mu^+\mu^-$, and the photon energies $\omega_{1,2}$ can be reconstructed from kinematic variables. The maximum energy of a colliding photon at the LHC with $\sqrt{s_{\mathrm{NN}}} = 5.36\,\mathrm{TeV}$ in Pb-Pb collisions is up to about $100\,\mathrm{GeV}$ [18].

$$\omega_{1,2} = \frac{1}{2} m_{\mu\mu} e^{\pm y}, \tag{10}$$

where $m_{\mu\mu}$ is the invariant mass of the muon pair, and y is their rapidity. The experimental distributions $d\sigma/d\omega_{min}$ and $d\sigma/d\omega_{max}$ ($\omega_{min} = \min[\omega_1, \omega_2]$, $\omega_{max} = \max[\omega_1, \omega_2]$) [19] are shown in Figure 9 as the projections of the theoretical EPA convolution onto the kinematic variables of photons.

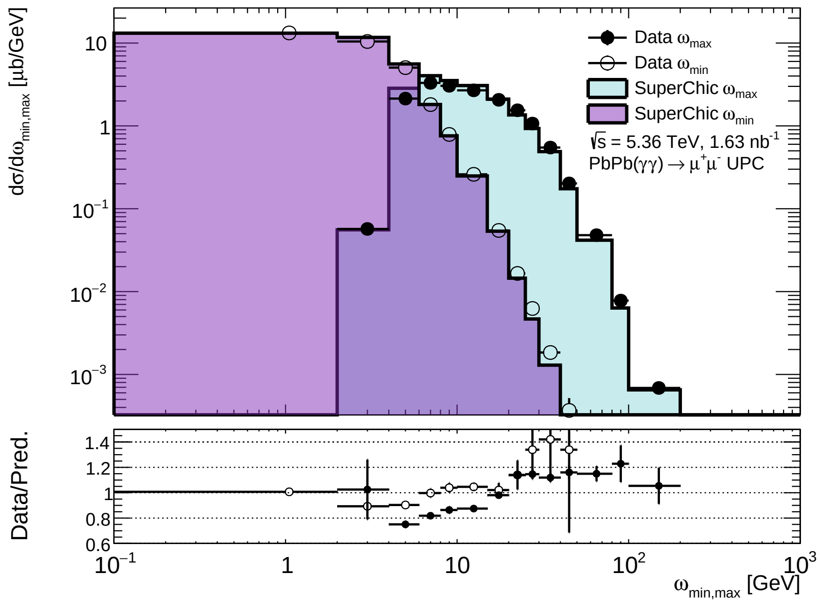

Figure 9: Differential cross sections for the $\gamma\gamma \rightarrow \mu\mu$ process $d\sigma/d\omega_{min,max}$ as a function of minimum/maximum photon energy. The distributions are produced after the selection described in Section

UPC provides a clean environment for studying EM interactions due to the suppression of the hadronic background resulting from strong interactions. An exception is the EM dissociation (EMD): a strong EM field can excite another nucleus, which then emits one or more forward neutrons at small polar angles relative to the beam (inclusive production). Dimuon pairs arise from the coherent or incoherent photoproduction of vector mesons (e.g J/ψ, Υ) following their decay to $\mu^+\mu^-$, or from exclusive two-photon scattering to muon pairs, precisely described by quantum electrodynamics (QED) theory. The two muons are produced roughly back-to-back ($\Delta\phi \approx \pi$), with similar values of transverse momentum, resulting in a small p_T of the muon pair.

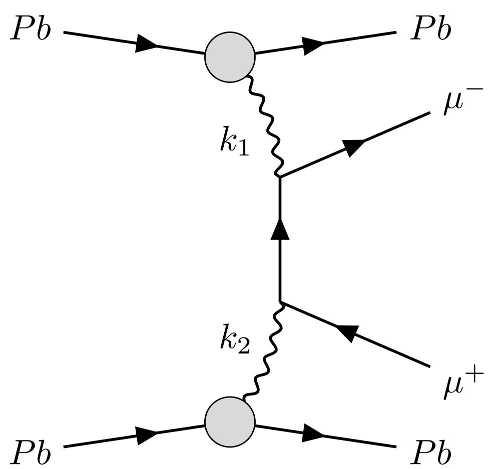

Figure 10: Leading order Feynman diagram of dimuon production in UPC

Neutrons originating from the EMD are detected in the ATLAS Zero Degree Calorimeters (ZDCs), located at a distance of about 140 m on both sides (A - positive and C - negative) of the IP. There are four different event classes in ZDC: 0n0n, XnXn, 0nXn, and Xn0n; where "0n" stands for the lack of neutron activity on one side of the IP, and "Xn" has the opposite meaning.

In this thesis, all four classes are taken into account; in the dataset used, the most numerous class is the 0n0n.

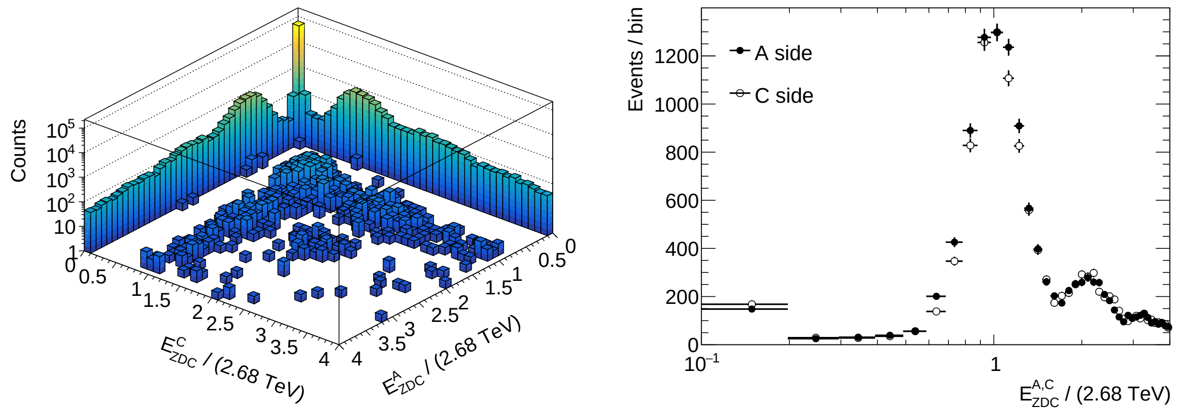

Figure 11: (left) Energy correlation between both sides normalised to the beam energy in ZDC. (right) Energy distribution for both sides of ZDC normalized to the beam energy

The energy of emitted neutrons along the beam direction is approximately equal to the beam energy. The ZDC energy is therefore normalised to the beam energy to express the signal in units of detected neutrons. Both distributions are produced after applying the event selection described in Section 3.2.

2.8 Dataset and Monte Carlo samples

The dataset used in this analysis comes from UPC 2023 Pb+Pb (Run 3) with an integrated luminosity $L_{int} = 1.63\,\mathrm{nb}^{-1}$. Luminosity L is the number of particles in the beam per unit surface per unit time for two counter-propagating relativistic beams, luminosity is defined as

$$L = fn\frac{N_1 N_2}{A}, \tag{11}$$

where f corresponds to the frequency of colliding particles, n is the number of bunches per beam, N_i is related to the number of particles in the bunch, and A is the cross-sectional area. Integrated luminosity is the integral with respect to time $L_{int} = \int L\, dt$, and it provides data on the total number of interactions per unit cross section.

In every particle physics analysis, there is a need to generate Monte Carlo (MC) simulations. MC samples facilitate the corroboration of data and the estimation of the background for specific processes or for calibration. For this analysis, the SuperChic [20] generator is used, interfaced with Pythia8. The SuperChic generator produces central exclusive and photon-initiated events in proton-proton and heavy-ion collisions. In this thesis (Pb+Pb) $\gamma\gamma \rightarrow \mu\mu$ processes are generated. The QED theory predicts that produced leptons might emit a photon. To achieve this, the output of the SuperChic generator is interfaced to Pythia8, where the QED final-state radiation (FSR) is simulated. The FSR smears the dilepton invariant mass spectrum and produces the tail of the acoplanarity distribution. The SuperChic generator is found to provide well-shaped distributions of the kinematic variables, but it overestimates the cross-section [21].

The generated samples are divided into three groups based on the invariant mass of the muon pairs: 4-7 GeV (4M7), 7-20 GeV (7M20), and above 20 GeV (20M), with each sample consisting of 50000 events. During the analysis, a problem with the MC simulation was identified: the MC samples have been generated only in the 0n0n ZDC category. This issue was corrected, and all subsequent analyses were performed with the updated MC sample.

3 Event selection and MC normalisation

Any physical experiment must have a dedicated selection of data to distinguish the signal from the background processes. The NTUPLE object in ATLAS is a previously skimmed dataset that contains only the necessary information about each event. It helps analyse the data on the personal computer because it takes up less memory.

3.1 Preselection

The preselection of the dataset already requires every event to pass the Good Run List (GRL) condition, so it does not have any impact on the nominal selection, as can be observed in Table 1. The GRL selects only good-quality events which were recorded with the detector fully operational.

3.2 Signal selection

At the very beginning of the selection, there is a requirement for the fired `HLT_mu3_L1MU3V_VTE50` trigger (more details about this trigger are provided in Section 4.). Due to the nature of the process $\gamma\gamma \to \mu^+\mu^-$, the number of muons must be equal to two, and both must have opposite charges. The transverse momentum is greater than 3 GeV, and the absolute value of the pseudorapidity is less than 2.5. The working point of `muon_is_LowPt` or `muon_is_Loose` is an identification criterion. The acoplanarity ($A_\phi^{\mu,\mu} = 1 - \Delta\phi(\mu,\mu)/\pi$), where $\Delta\phi(\mu,\mu)$ is defined as $\Delta\phi = |\phi_1 - \phi_2|$ for $\phi_1 > \phi_2$, must be less than 0.01. Nearly back-to-back production in UPC is the reason for this selection cut. To suppress the number of muons from cosmic rays, the absolute value of [1] transverse impact distance (d_0) has to be lower than 1.1 mm.

Cut	Number of events
All events	1489893
At least one muon	414100
Passed GRL	414100
Passed trigger	401566
Exactly 2 muons with $p_T > 3$ GeV and $\lvert\eta\rvert < 2.5$	129551
LowPt or Loose identification criteria	116169
Opposite charges	115667
$A_\phi^{\mu,\mu} < 0.01$	103014
$\lvert d_0\rvert < 1.1$ mm	102823

Table 1: The selection criteria described in Section 3.2 and numbers of events passing them in the data

Table 1 shows quantitatively how many events are selected after each cut. The most impactful criterion is associated with transverse momentum and pseudorapidity, as it vetoes roughly 68% of events. The total number of events is equal to 102823 providing satisfactory statistics.

3.3 MC normalisation

To compare the number of events and the shapes of distributions of various kinematic variables between data and MC for an integrated luminosity L_{int} of data and the specific process cross section (σ), the normalisation procedure is a crucial step. The normalisation process is carried out using weights (w), where each MC event is scaled by this factor

[1] The transverse impact parameter d_0, defined as the closest approach from a charged particle track to the primary vertex in the transverse plane x-y of the beam axis

$$w = \frac{L_{int} \cdot \sigma}{N_{MC}}, \tag{12}$$

The MC samples are separated into three groups, each with a corresponding cross section value: $\sigma_{4M7} = 925\,\mu b$, $\sigma_{7M20} = 265\,\mu b$, and $\sigma_{20M} = 9.74\,\mu b$. The integrated luminosity of the data is equal to $1630.29\,\mu b^{-1}$, N_{MC} denotes the total number of events in the MC sample, and in this analysis $N_{MC} = 50000$ for each sample. The values of the calculated weights are: $w_{4M7} = 30.16$, $w_{7M20} = 8.64$, $w_{20M} = 0.32$.

	Number of events			
Cut	4M7	7M20	20M	Total
All events	50000	50000	50000	150000
At least one muon	8723	31390	48510	88623
Passed GRL	8723	31390	48510	88623
Passed trigger	339	13251	39576	53166
Excatly 2 muons with $p_T > 3\,\text{GeV}$ and $\lvert\eta\rvert < 2.5$	148	11785	36204	46562
LowPt or Loose identification criteria	117	11111	35303	46531
Opposite charges	117	11111	35302	46530
$A_{\phi}^{\mu,\mu} < 0.01$	117	10857	33820	44794
$\lvert d_0\rvert$ <1.1 mm	117	10855	33817	44789

Table 2: The selection criteria described in Section 3.2 and numbers of events passing them in MC simulation

The identical selection as for the data (Section 3.2) is applied to the MC samples. In contrast to the data, the most stringent requirement is the trigger selection. The opposite-sign requirement and the transverse impact-parameter requirement do not affect the MC samples, because only opposite charges are simulated, and cosmic-ray muons are absent. The trigger selection rejects about 75% of events, overall, there are 44789 events. Table 2 presents the discussed selection results.

3.4 Control plots

In order to validate distribution shapes or trends, the count of events, error diagnostics, and selection of thresholds or parameters, there is a common practice of producing control plots containing simple-to-interpret kinematic variables. In this analysis, kinematic variables such as pseudorapidity, transverse momentum, acoplanarity, azimuthal angle, and the invariant mass of the muon pair are used for the validation of data and MC samples.

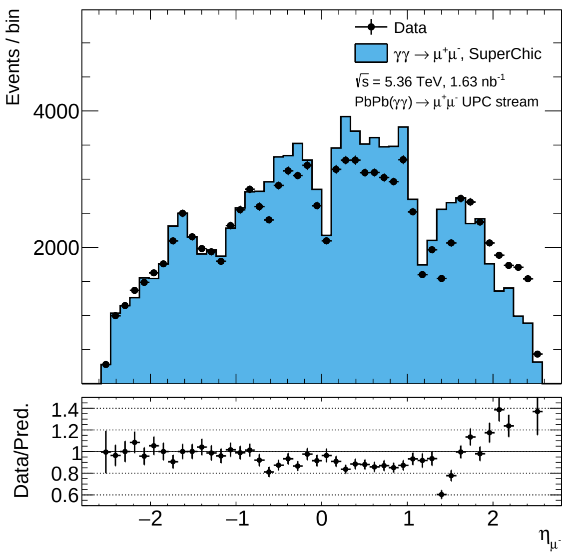

(a) Negatively charged

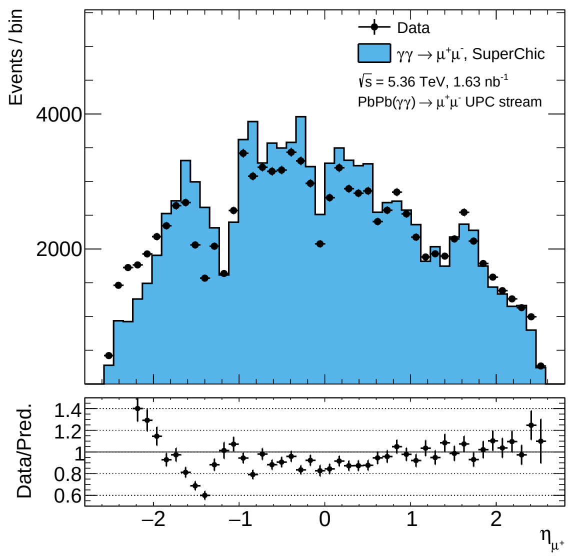

(b) Positively charged

Figure 12: Pseudorapidity distribution of the positively and negatively charged muons. Bottom panels shows data-to-MC ratios. Error bars represent statistical uncertainties on the ratio

In Figure 12, based on the previous studies of dielectrons [21], the expected value of the ratio (bottom panel) is between 0.8 and 1. It can be observed that at the edges of both distributions, the discrepancies are much larger, probably due to the MC mismodeling.

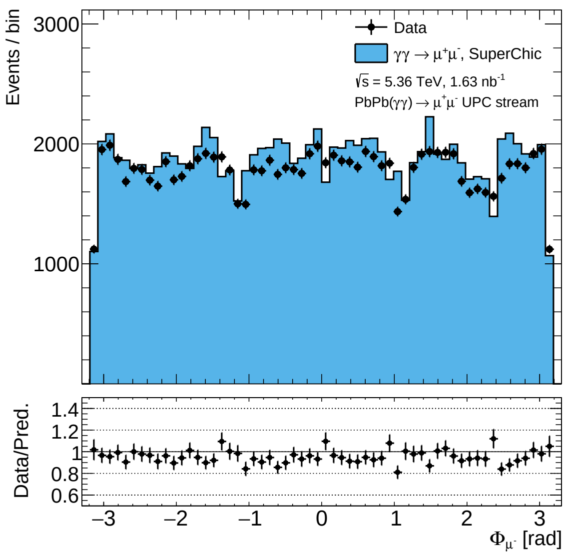

(a) Negatively charged

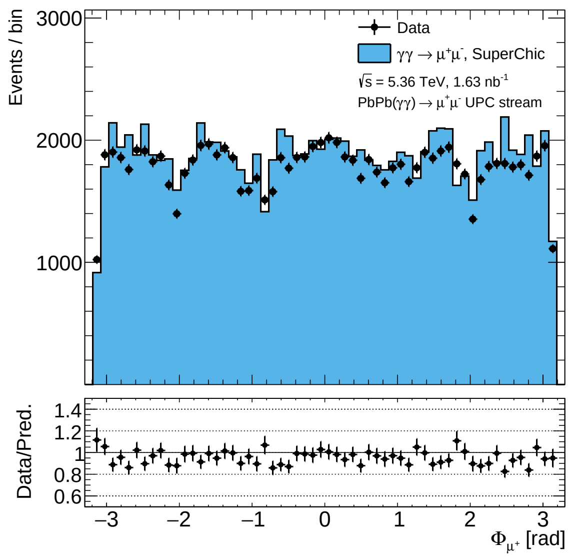

(b) Positively charged

Figure 13: Azimuthal angle distribution of the positively and negatively charged muons. Bottom panels shows data-to-MC ratios. Error bars represent statistical uncertainties on the ratio

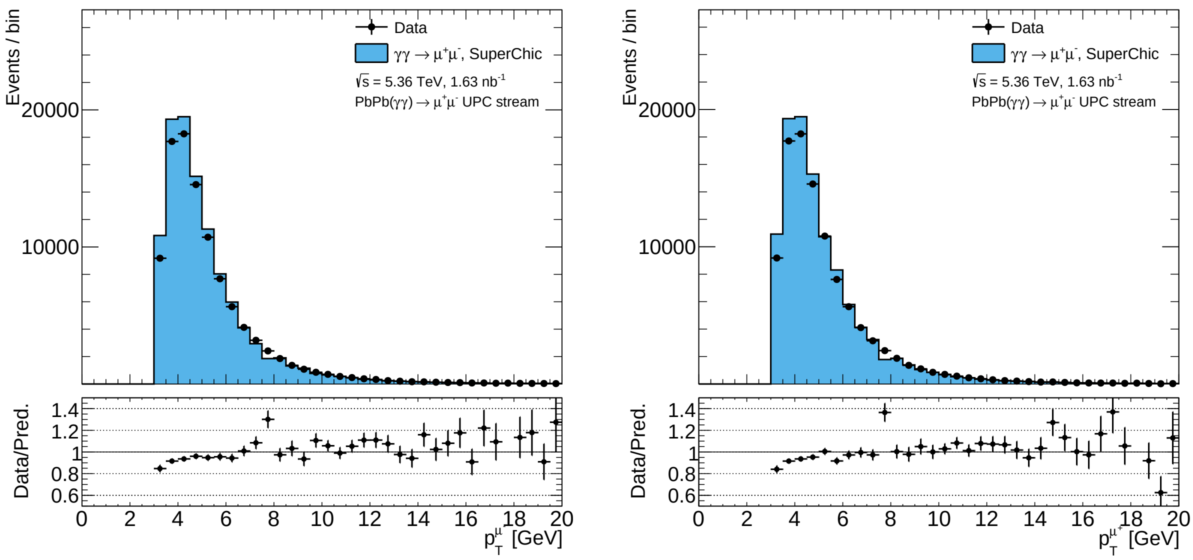

(a) Negatively charged

(b) Positively charged

Figure 14: Transverse momentum distribution of the positively and negatively charged muon. Bottom panels shows data-to-MC ratios. Error bars represent statistical uncertainties on the ratio

In Figure 14, one can observe that the data contain more entries than MC, roughly 35% more in the 7-8 GeV bin. This analysis did not investigate that issue further. A more detailed analysis will be needed in the future.

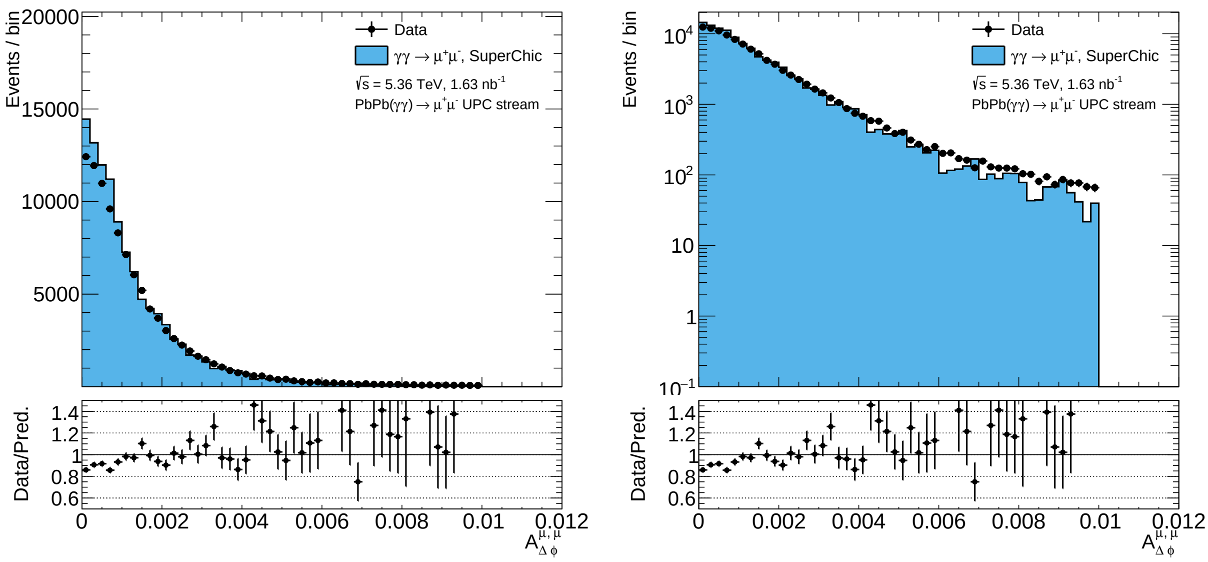

(a) Linear scale

(b) Logarithmic scale

Figure 15: Acoplanarity distributions of the muon pairs in two different scales (a) linear, (b) logarithmic. Bottom panels shows data-to-MC ratios. Error bars represent statistical uncertainties on the ratio

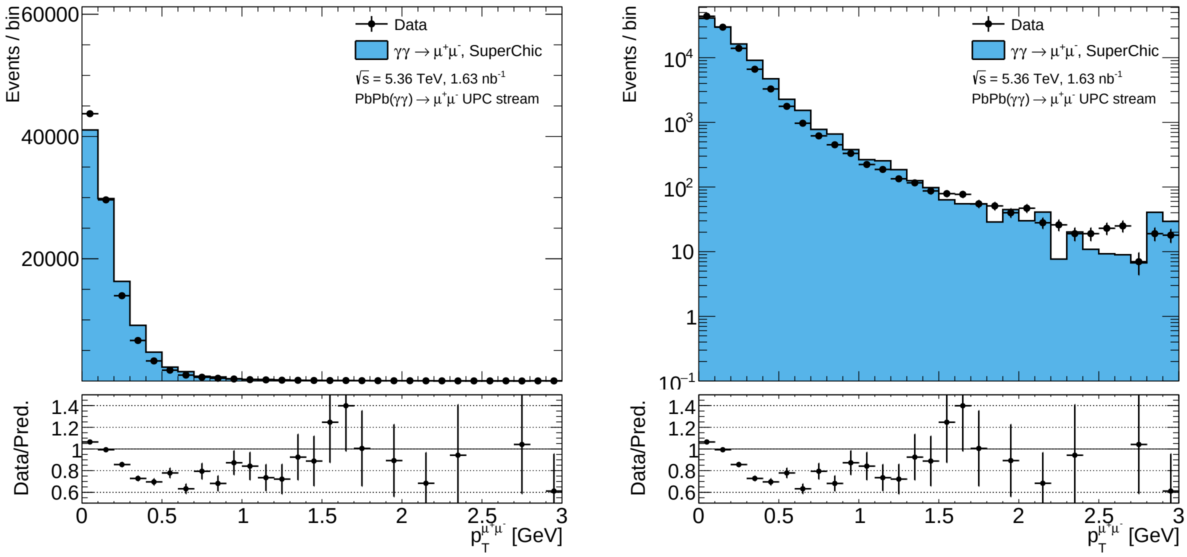

(a) Linear scale

(b) Logarithmic scale

Figure 16: Transverse momentum distributions of the muon pairs in two different scales (a) linear, (b) logarithmic. Bottom panels shows data-to-MC ratios. Error bars represent statistical uncertainties on the ratio

Figure 16 shows the distribution of $|\mathbf{p}_T^{\mu\mu}|$. Differences in shapes between the data and MC simulation are visible. The reason for the different shapes between the data and the MC simulation is currently unknown; a similar behavior is also observed in the MC samples for the process of $\gamma\gamma \to e^- e^+$. The investigation of this issue is currently in progress. Initial indications might point to a problem in the generator stage of MC production.

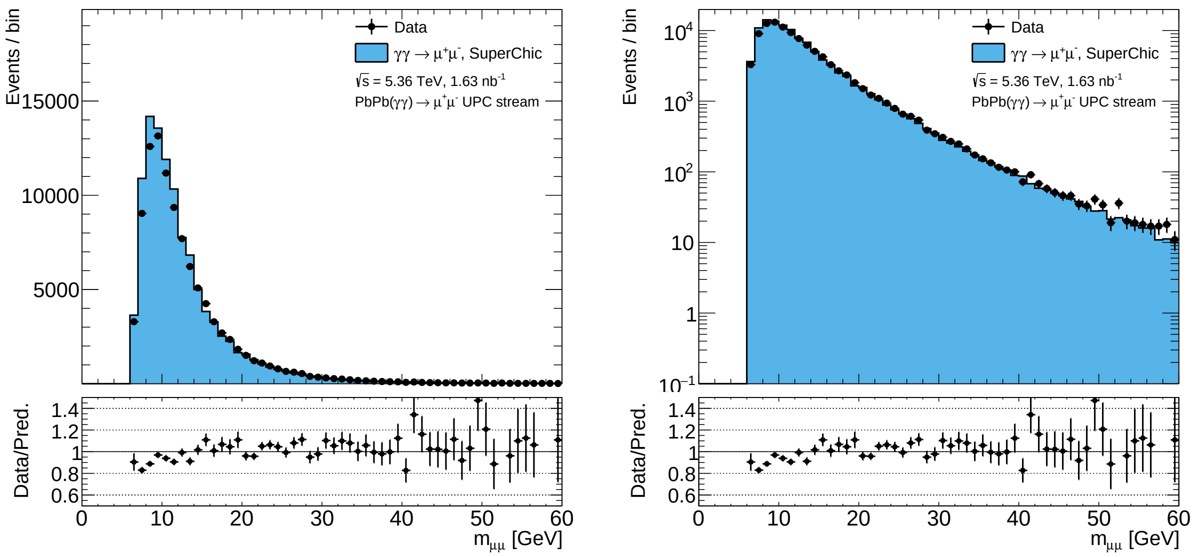

(a) Linear scale

(b) Logarithmic scale

Figure 17: Invariant mass distributions of the muon pairs in two different scales (a) linear, (b) logarithmic

Overall, the control plots (Figures 12-17), despite a few mismatches, look reasonable and can be applied in further analysis. The identified discrepancies between the MC simulation and the data do not affect the determination of the trigger efficiency.

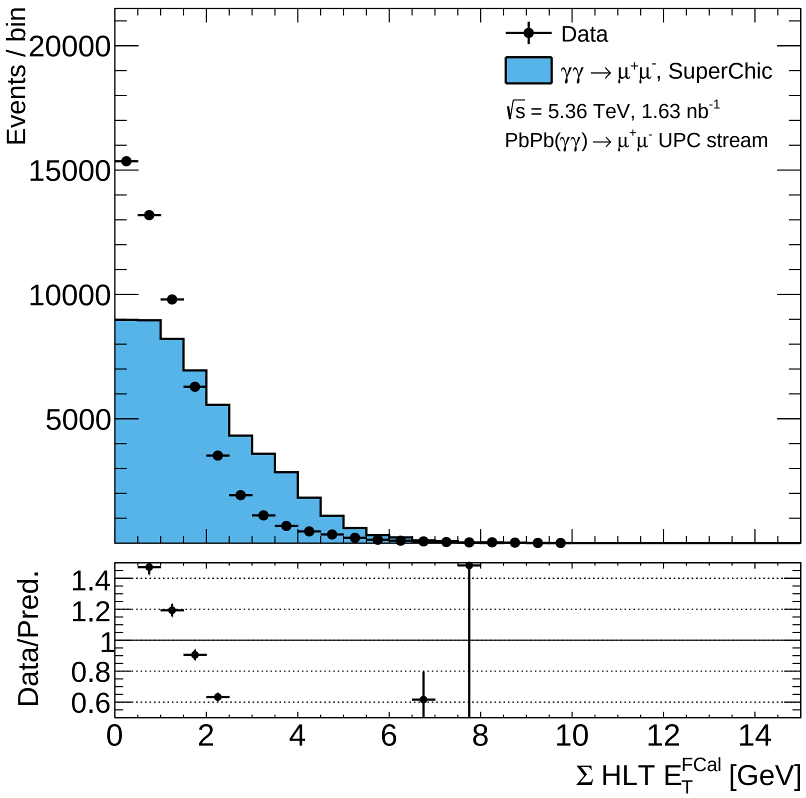

Figure 18: The transverse energy deposited in the FCal calculated in the HLT system

The distribution of HLT E_T^{FCal} in Figure 18 shows a poor agreement of the data with MC simulation, despite the lack of exclusive dimuon selection [19] for $\gamma\gamma \rightarrow \mu\mu$; The MC simulation indicates a larger activity in the FCal than the data in the 2-6 GeV region. The possible sources of such discrepancies may vary, e.g., a model mismatch of nuclear dissociation, a soft hadronic activity, and an invalid model of HLT/FCal. They need to be studied further in the future analysis of the HLT trigger efficiency of the FCal requirement.

3.5 Comparisons to the previous MC samples

In Figures 19-21, a side-by-side comparison of the previously generated MC samples for the 0n0n category and the nominal MC samples is shown. Based on the previous studies [21], the SUPERCHIC-generated contribution is expected to lie systematically above the data yield. The root cause was the 0n0n setting used in MC production, which indicates that the distributions of the kinematic variables were disturbed. Identifying and fixing this problem was essential for proceeding with further analysis.

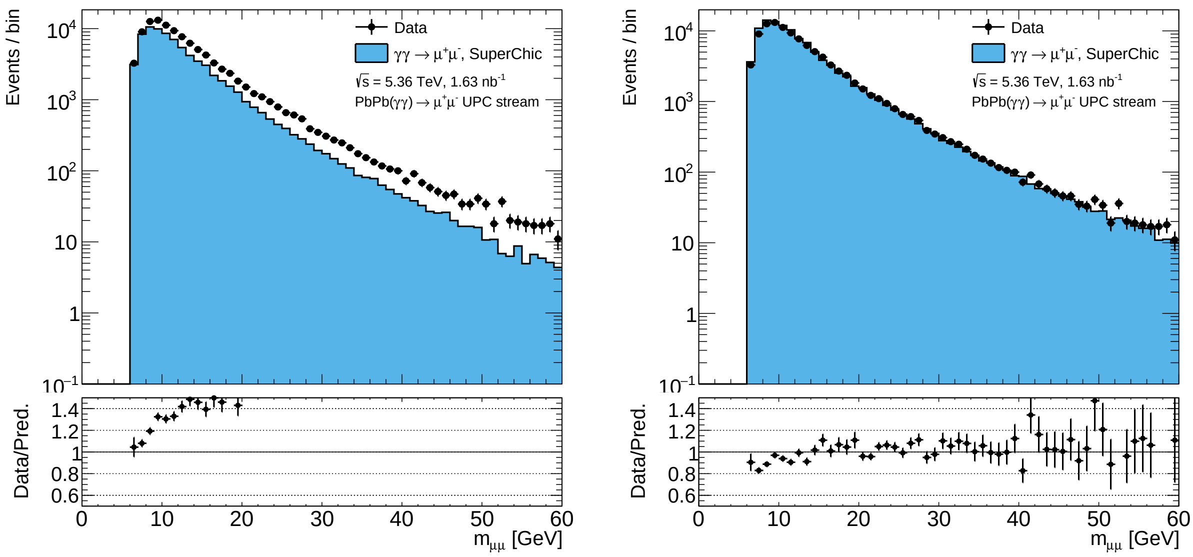

Figure 19: The invariant mass distributions in the logarithmic scale for (left) the old MC production for the 0n0n category, and (right) for nominal MC production

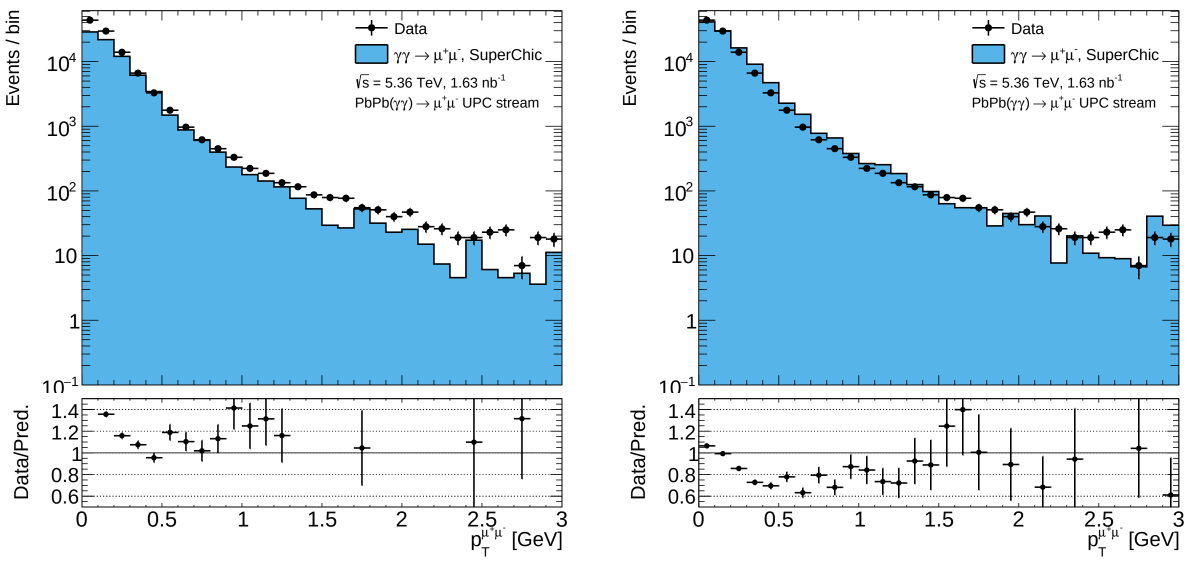

Figure 20: The distributions of muon pair transverse momentum in the logarithmic scale for (left) the old MC production for the 0n0n category, and (right) for nominal MC production

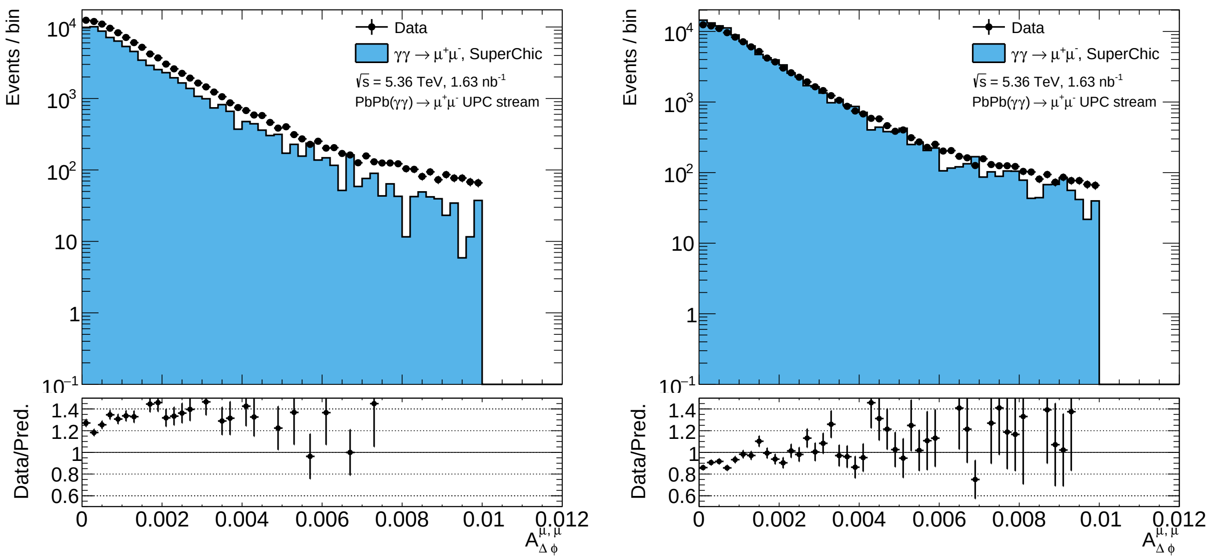

Figure 21: The acoplanarity distribution in the logarithmic scale for (left) the old MC production for the 0n0n category, and (right) for nominal MC production

4 The ATLAS muon trigger

The interaction rates of pp and Pb+Pb collisions are roughly equal to 1 GHz and 7.7 kHz [22], respectively, making it impossible to record all this data. To optimise the amount of data acquired in ATLAS, the dedicated ATLAS trigger system is employed. Two levels of triggers can be distinguished: the hardware based First-Level Trigger (L1) and the software based High-Level Trigger (HLT). The L1 trigger utilizes only certain parts of the detector, such as calorimeters or muon chambers, it reduces the event rate to 100 kHz. The muon trigger system uses RPC from the barrel region ($|\eta| < 1.05$) and TGC from the endcaps ($1.05 < |\eta| < 2.4$); the entire coverage is then for $|\eta| < 2.4$. The L1 trigger operates within a constant latency time of 2.5 µs and then decides whether the event is worth accepting or rejecting. Accepted events are passed to HLT, where more sophisticated algorithms are applied to reconstruct the track based on information from the ID and MS or to compute the estimation of transverse momentum. This process reduces the event rate from 100 kHz to 3 kHz. In the last resort, the HLT decides whether the event is saved in disk storage.

4.1 Tag and probe method

Trigger efficiency (ε) quantitatively verifies what fraction of events that satisfy the physical criteria are actually recorded by the trigger system. The standard method for calculating the trigger efficiency is the Tag and Probe method. One muon must fulfill strict criteria (tag), and the other muon (probe) is an independent object on the basis of which trigger efficiency is calculated. The efficiency can be calculated as a function of p_T, $q\eta$ (q is the charge of the particle) or θ. The method can be applied to data and MC simulation.

In this analysis, the tag object must be a well reconstructed muon with an offline working point `muon_is_Tight`, an absolute value of pseudorapidity $|\eta| < 2.4$ (the muon trigger system coverage), and must satisfy the matching criteria $\Delta R < 0.3$ with the L1 muon trigger (Subsection 4.1.1). After identifying the tag, the efficiency can be computed using the formula below

$$\varepsilon(x) = \frac{N_{(\mathrm{probe}|\Delta R<0.3)}}{N_{\mathrm{probe}}}. \tag{13}$$

$N_{(\mathrm{probe}|\Delta R<0.3)}$ stands for the number of probes that have passed the matching criteria of $\Delta R < 0.3$, N_{probe} is the total number of probes, and x represents a generic observable (e.g. p_T, $q\eta$, θ) with respect to which the efficiency is measured. In the event that both muons pass the tag criteria, both of them are also taken into consideration.

4.1.1 Trigger matching criteria

This thesis investigates the efficiency of the L1_MU3V_VTE50 muon trigger, which was saving muons with $p_T > 3$ GeV (MU3V), a requirement on transverse energy (E_T) in the calorimeter that is less than 50 GeV (VTE50).

To verify whether the offline reconstructed muon is the originating muon saved in the L1 muon trigger, the matching criteria $\Delta R(\mu_{reco}, \mu_{L1})$ are applied between them.

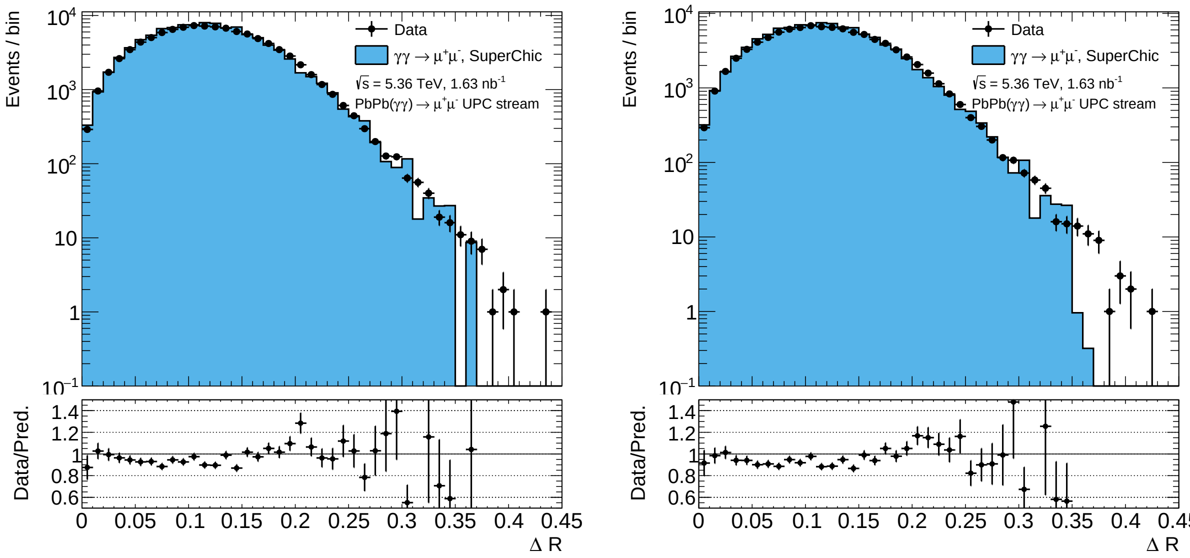

(a) Angular distance distribution between tag and L1 muon. Logarithmic scale

(b) Angular distance distribution between probe and L1 muon. Logarithmic scale

Figure 22: Angular distance distributions

Figure 22 represents the angular distance between the L1 muon and the tag (a), and probe (b). A detailed comparison between data and MC simulation is shown in the ratio panel. A good agreement is found. Based on these distributions, the matching criteria are set to $\Delta R < 0.3$.

4.2 Trigger efficiency results

This subsection focuses on the results of the calculated efficiency of the L1_MU3V_VTE50 muon trigger by applying the tag and probe method to the analysed dataset. Trigger efficiencies are estimated as a function of p_T and $q\eta$. All of the presented plots with efficiencies have irregular binning in order to balance statistical uncertainties across the entire data range. The efficiencies and their uncertainties are estimated using the Clopper-Pearson method by the ROOT framework automatically.

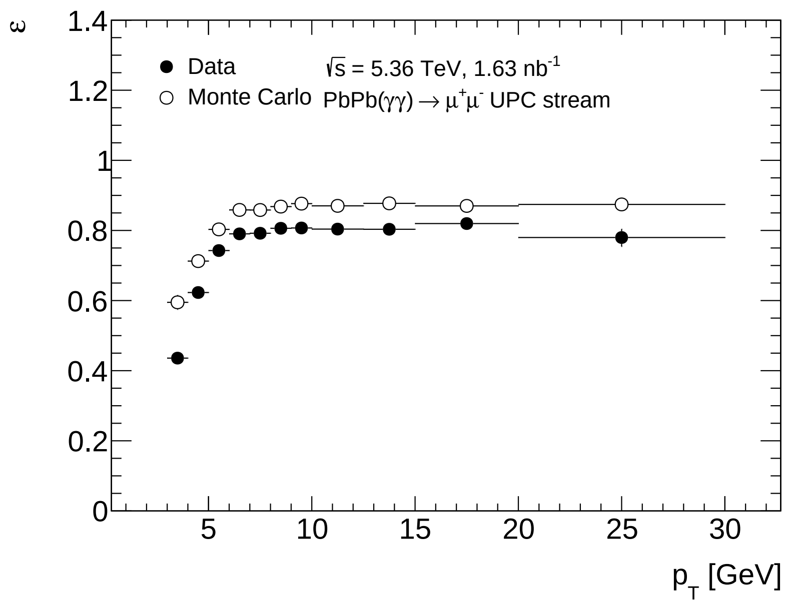

Figure 23: Trigger efficiency as a function of p_T in the full $|q\eta| < 2.4$ spectrum in data (full points) and MC simulation (open circles)

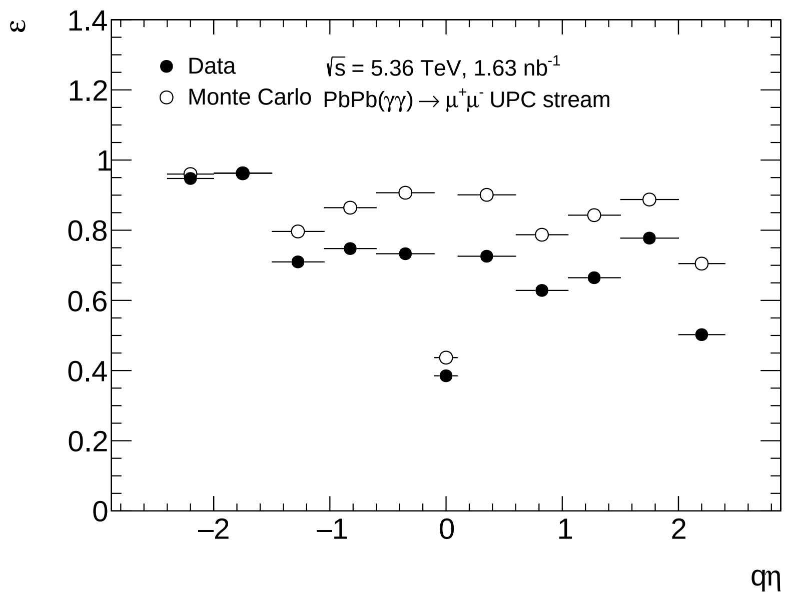

Figure 24: Trigger efficiency as a function of $q\eta$ in the full $p_T > 3$ GeV spectrum in data (full points) and MC simulation (open circles)

Discrepancies between the data and the MC simulation are observed in both Figures 23 and 24. In Figure 23, the trigger efficiencies measured in the data are systematically lower than those obtained from the MC simulation. In Figure 24, the differences are asymmetric: in the $-2.4 < q\eta < -1.5$ interval, the data and MC are in good agreement, while in the residual $q\eta$ intervals, noticeable discrepancies are visible. In Figure 23, the p_T dependence of trigger efficiency at the low value of p_T increases and reaches a plateau level around p_T of 7 GeV, in agreement with the ATLAS measurements of the performance of the ATLAS muon triggers in Run 2 [23]. The second graph likewise represents the L1 trigger efficiency as a function of $q\eta$; the reason for the asymmetry will be explained in more detail later in this work. A geometrical gap between the barrel and the endcap muon system in the region $1.0 < |\eta| < 1.3$ leads to reduced trigger efficiency in this pseudorapidity range. The measurements are performed with high statistical precision. The statistical uncertainties in most of the bins are smaller than the marker size.

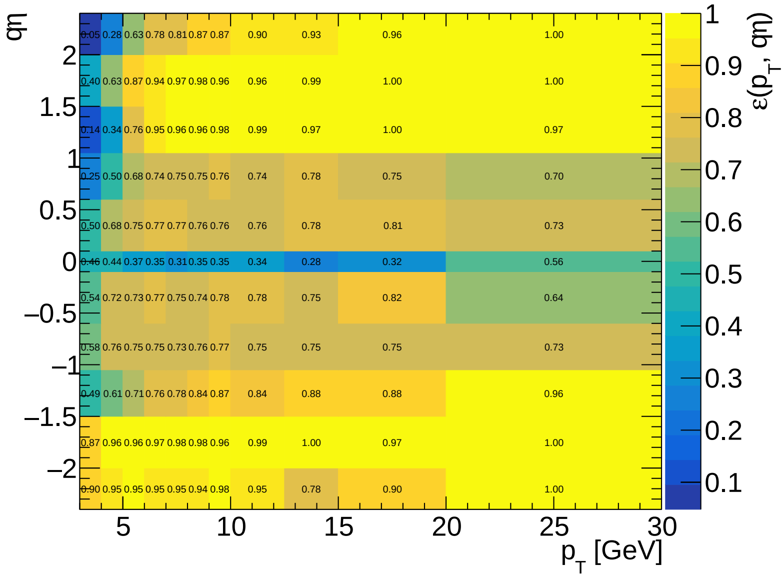

Figure 25: The map of L1 trigger efficiency $\varepsilon(p_T, q\eta)$ for the data

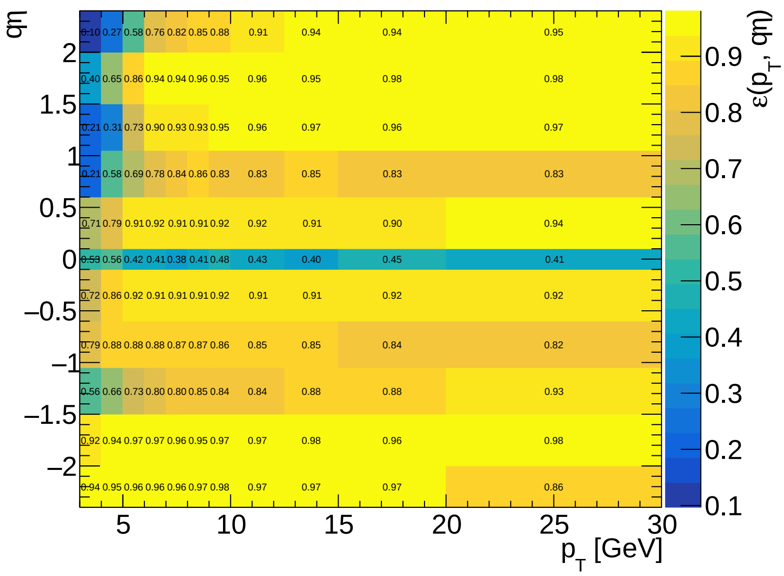

Figure 26: The map of L1 trigger efficiency $\varepsilon(p_T, q\eta)$ for the MC simulation

Both the data and MC simulation in Figures 25-26 show that in the barrel region ($|\eta| < 1.05$) of the detector, L1 trigger efficiencies are lower than in the endcap region ($1.05 < |\eta| < 2.4$). This is due to the differences in the L1 trigger coverage for the barrel region (~80%) and the endcap region (~99%) [23]. The lowest values of efficiencies are observed for $|\eta| < 0.1$ due to the detector gap that provides space for the ID and calorimeter services. This feature is reproduced by MC simulation.

Figures 27-32 illustrate the projections of the trigger efficiency maps of Figures 25-26 in individual $q\eta$ bins. The agreement in the central region between the data and the MC simulation is clearly worse than that in the forward region. The trigger efficiency for data in the barrel is approximately equal to 0.8, except for the $-0.1 < q\eta < 0.1$ region where it amounts to 0.4, whereas the efficiency in the endcap is higher, reaching 0.9-1. In addition, for $q\eta < 0$, the efficiencies reach a plateau almost instantly, even for low p_T muons, in contrast to the efficiencies for $q\eta > 0$. Precision

During Run 2, to eliminate the fake muons originating mainly from low-p_T hadrons, such as protons or pions produced in the toroid and beam shielding, an additional requirement for coincidence between the Big Wheel, the TGC Forward Inner (TGC-FI), and the TGC Endcap Inner (TGC-EI) was implemented. The Coincidence Windows (CWs) are distributed chamber-by-chamber, and they are configured in a fixed way so that most fake muons are suppressed while real muons still pass with high efficiency. The toroidal magnetic field and the detector geometry are not perfectly symmetric, the optimization results in somewhat different acceptance for real muons in the $q\eta < 0$ and $q\eta > 0$.

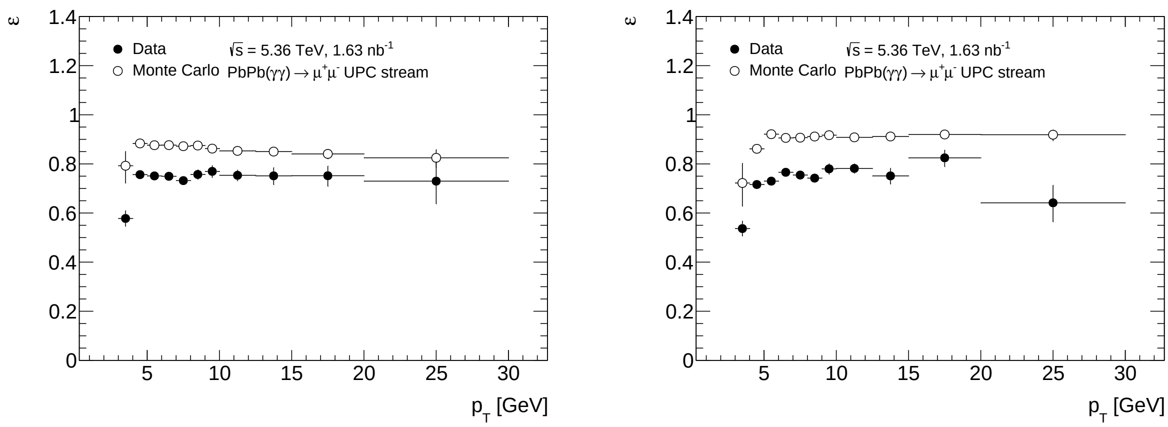

(a) -1.05 $< q\eta <$ -0.6 (b) -0.6 $\leq q\eta <$ -0.1

Figure 27: Trigger efficiency as a function of p_T - barrel region in data (full points) and MC simulation (open circles). Error bars represent statistical uncertainties

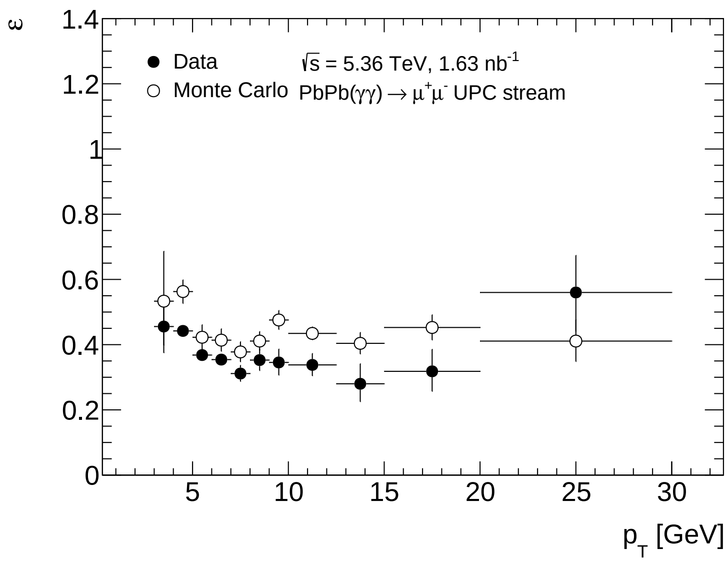

Figure 28: Trigger efficiency in the central region of barrel, -0.1 $< q\eta <$ 0.1, in data (full points) and MC simulation (open circles). Error bars represent statistical uncertainties

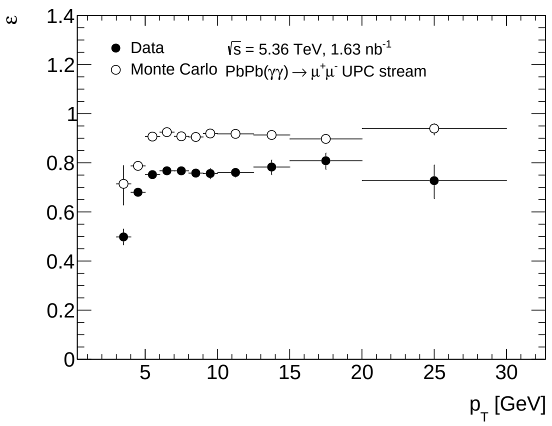

(a) $0.1 < q\eta < 0.6$

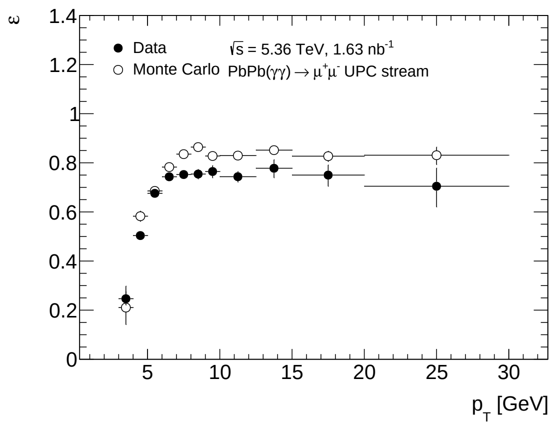

(b) $0.6 \leq q\eta < 1.05$

Figure 29: Trigger efficiency as a function of p_T - barrel region in data (full points) and MC simulation (open circles). Error bars represent statistical uncertainties

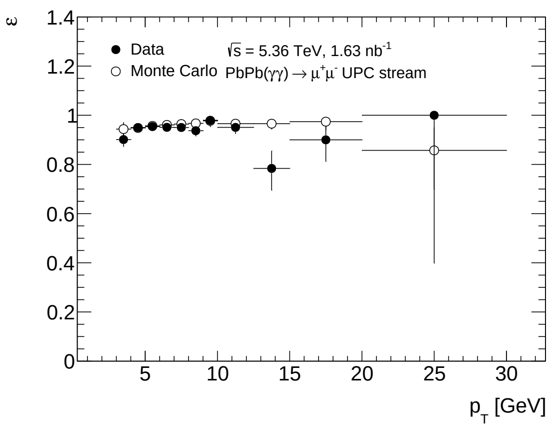

(a) $-2.4 < q\eta < -2$

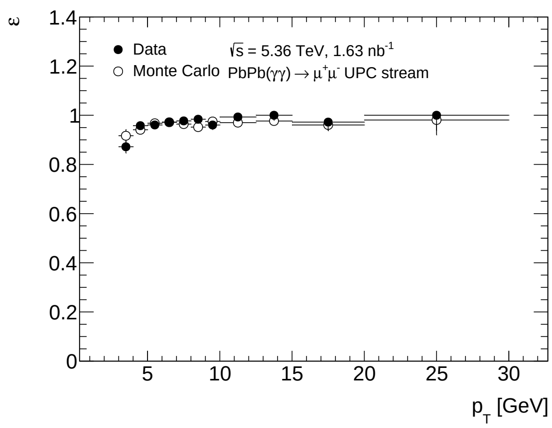

(b) $-2 \leq q\eta < -1.5$

Figure 30: Trigger efficiency as a function of p_T - endcap region in data (full points) and MC simulation (open circles). Error bars represent statistical uncertainties

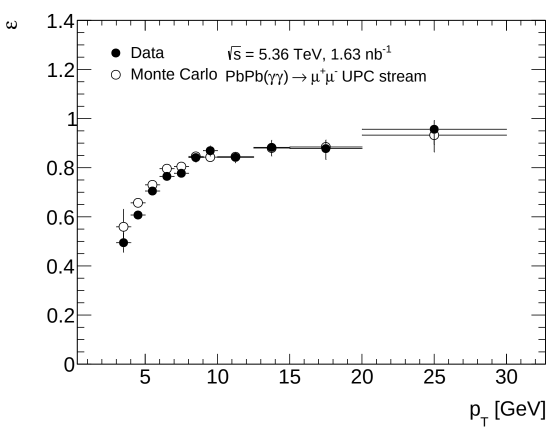

(a) $-1.5 < q\eta < -1.05$

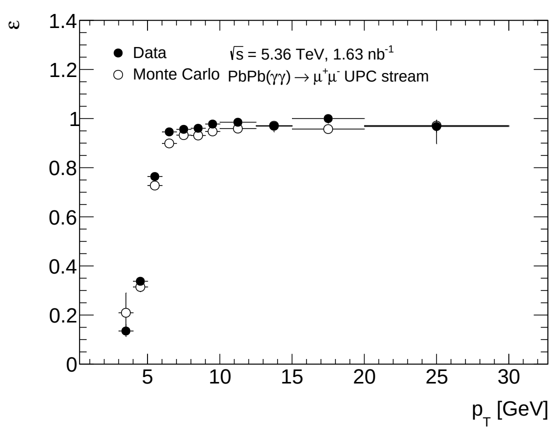

(b) $1.05 \leq q\eta < 1.5$

Figure 31: Trigger efficiency as a function of p_T - endcap region in data (full points) and MC simulation (open circles). Error bars represent statistical uncertainties

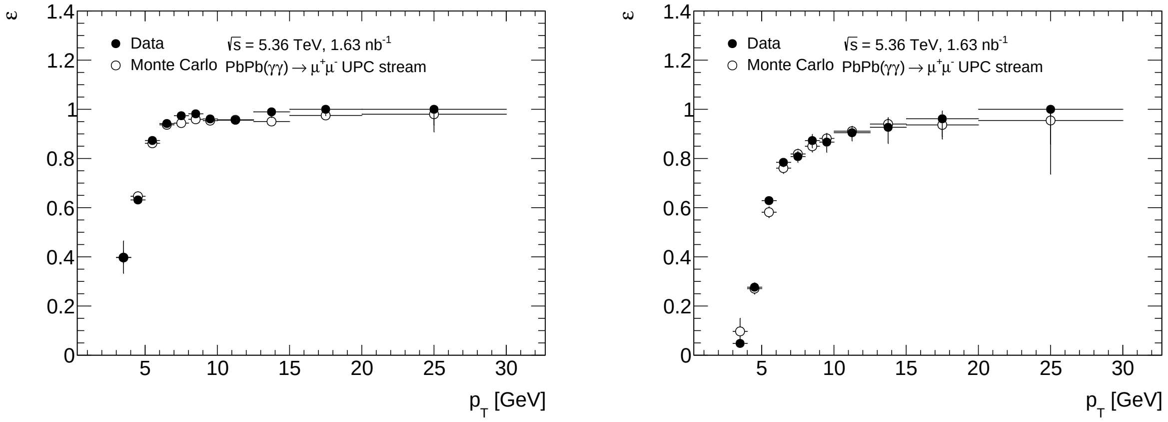

(a) $1.5 < q\eta < 2$

(b) $2 \leq q\eta < 2.4$

Figure 32: Trigger efficiency as a function of p_T - endcap region in data (full points) and MC simulation (open circles). Error bars represent statistical uncertainties

5 Scale factors

The efficiency scale factors (SF) are defined as a ratio between the trigger efficiency measured in data and the MC simulation.

$$\mathrm{SF} = \frac{\varepsilon_{data}(x)}{\varepsilon_{MC}(x)}, \ x \text{ represents a generic observable} \tag{14}$$

In case trigger efficiencies differ between data and MC simulation, they depart from unity. The origin of the difference might be mismodelling in MC simulation. The usefulness of these SFs is seen in the physics analyses; the MC simulations are scaled by this number to account for mismodelling and make trigger efficiencies similar in data and simulation.

5.1 The trigger efficiency SFs results

The values of SFs are lower in the barrel region, shown as a 2D maps in Figure 33, because the trigger efficiencies calculated for data are below the MC results (Figures 27-29). The better agreement between the trigger efficiencies for MC and data is shown in Figures 30-32; in the endcap region, the ratio is around the value of 1.

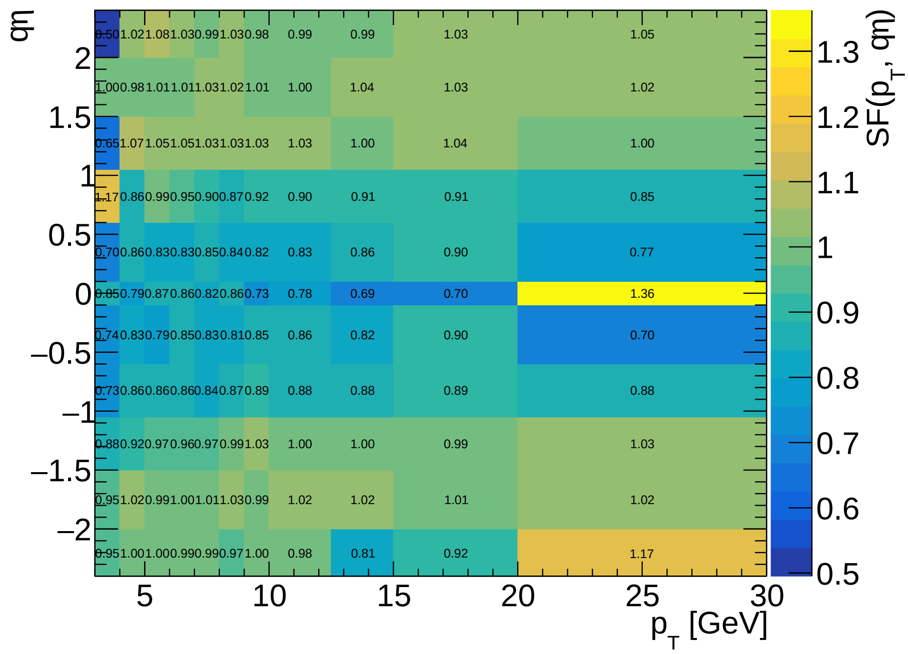

Figure 33: Estimated trigger efficiency scale factors as a function of p_T and $q\eta$

The statistical uncertainties on the SF values are propagated using the formula below

$$\sigma_{SF} = \sqrt{\left(\frac{\partial\,\mathrm{SF}}{\partial\varepsilon_{data}}\cdot\sigma_{\varepsilon_{data}}\right)^2 + \left(\frac{\partial\,\mathrm{SF}}{\partial\varepsilon_{MC}}\cdot\sigma_{\varepsilon_{MC}}\right)^2}, \tag{15}$$

this formula is applied separately for lower and upper uncertainties. Here, lower and upper uncertainties refer to asymmetric uncertainties obtained from a potentially asymmetric confidence interval computed using the Clopper-Pearson method.

Figures 34-39 show the 1D projections of the SF map from Figure 33 as a function of p_T in the individual $q\eta$ bins; the figures are divided into barrel and endcap regions. A constant model (0th order polynomial) is assumed and fitted to the data using the χ^2 minimization. In the presence of asymmetric uncertainties, the fit in the ROOT framework is accomplished using:

$$\sigma_i \equiv \begin{cases} \sigma_{i,\mathrm{up}}, & \text{if } y_{i,\mathrm{fit}} > y_i, \\ \sigma_{i,\mathrm{down}}, & \text{if } y_{i,\mathrm{fit}} < y_i. \end{cases} \tag{16}$$

where $\sigma_{i,up}$ ($\sigma_{i,down}$) is the upper (lower) error, $y_{i,fit}$ is the fitted value, and y_i is the data in the i-th point. The threshold of $p < 0.05$ is applied as a condition for more detailed diagnostics.[2] In Figure 34b, a standardized residual (pull) is estimated to reject the outlier ($\chi^2/\mathrm{ndf} \approx 1.899$ with $p \approx 0.0404$). The third point of this graph has **pull** ≈ 2.69; after rejecting this point, $p_T = (5, 6)$ GeV, the χ'^2/ndf drops to ~ 1.0426 and $p' \approx 0.4026$. Hence, the $p \approx 0.0404$ and $\chi^2/\mathrm{ndf} \approx 1.899$ in the nominal fit are not the result of the global trend, but rather the result of a single point.

To conduct a cross-check, the weighted mean value is calculated using the formulas below

$$\sigma_i = \sqrt{\frac{1}{2}\left(\sigma_{i,up}^2 + \sigma_{i,down}^2\right)}, \quad w_i = \frac{1}{\sigma_i^2}, \quad \overline{SF} = \frac{\Sigma_i w_i \cdot SF_i}{\Sigma_i w_i}, \quad \sigma_{\overline{SF}} = \sqrt{\frac{1}{\sum_i w_i}}. \tag{17}$$

In Eq. (17), σ_i is the symmetrized uncertainty, w_i is the weight, and $\overline{SF}$ is a calculated mean of SF with the uncertainty of $\sigma_{\overline{SF}}$. A good agreement of the results of the two methods (fit versus mean) within uncertainties leads to the conclusion that the asymmetric errors do not play a major role.

Figures 34-36 show that there is a need for SFs in the barrel region because, on average, SF values are most likely to be $\sim 0.8 - 0.9$. Similar conclusions were drawn in the Run 2 analysis presented in [24]. A possible explanation for this result is that the trigger might not be well modeled in this region. In the forward region (Figures 37-39), the average SF values appear to be better aligned with unity, varying between 0.95 and 1.05. Furthermore, assuming a constant function model shows that the SF value indicates no dependence on p_T.

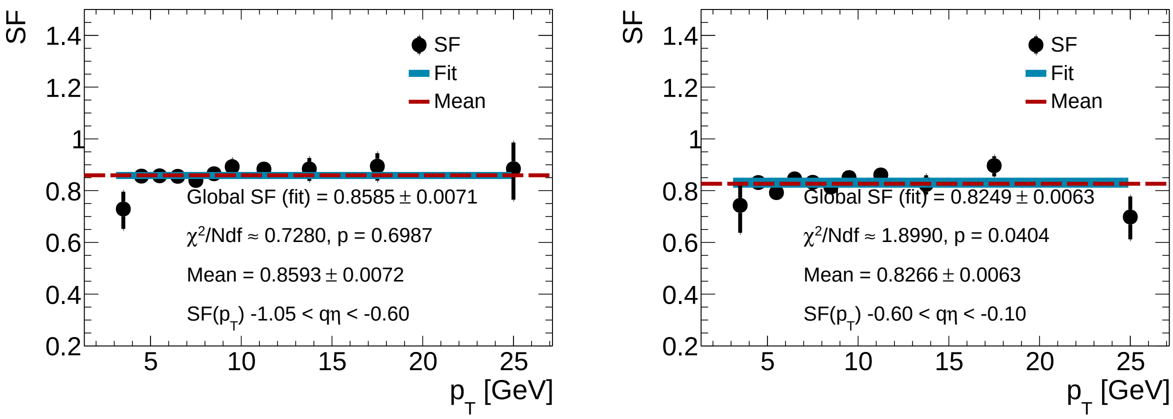

(a) -1.05 $< q\eta <$ -0.6

(b) -0.6 $\leq q\eta <$ -0.1

Figure 34: Trigger efficiency SFs as a function of p_T - barrel region

[2]The p-value is the probability of obtaining a test result at least as extreme as the observed result, assuming that the null-hypothesis is correct.

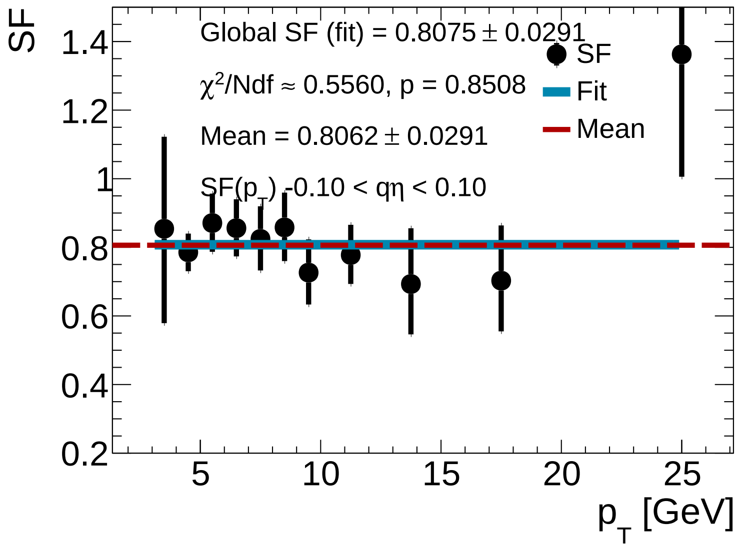

Figure 35: Trigger efficiency SFs as a function of p_T - barrel region, $-0.1 < q\eta < 0.1$

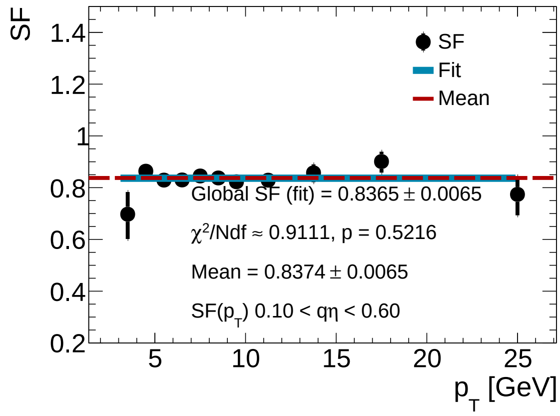

(a) $0.1 < q\eta < 0.6$

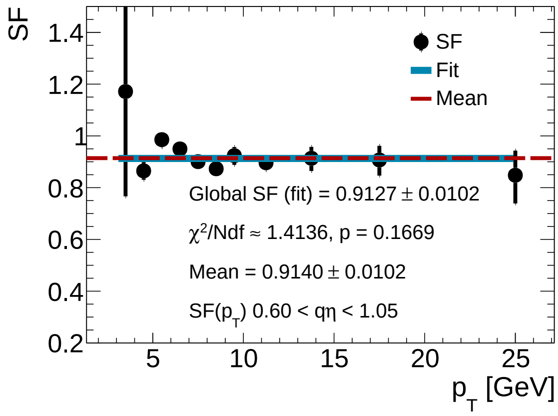

(b) $0.6 \leq q\eta < 1.05$

Figure 36: Trigger efficiency SFs as a function of p_T - barrel region

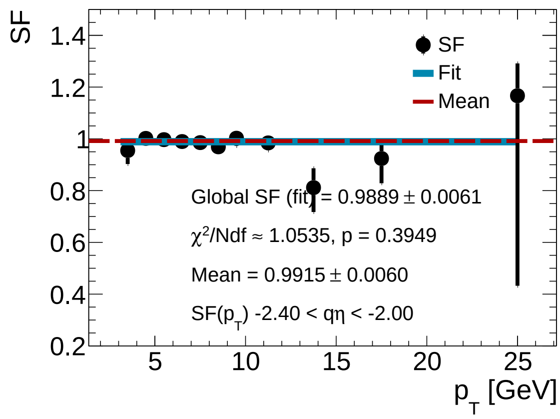

(a) -2.4 $< q\eta <$ -2

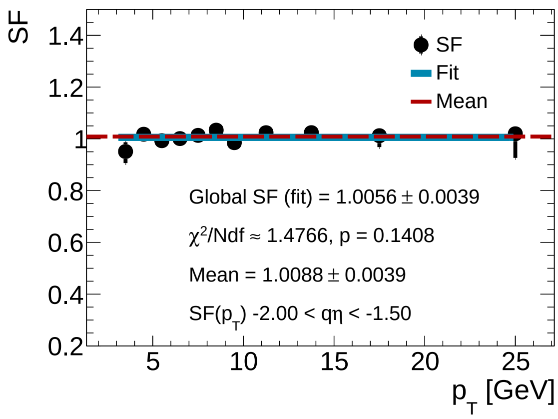

(b) -2 $\leq q\eta <$ -1.5

Figure 37: Trigger efficiency SFs as a function of p_T - endcap region

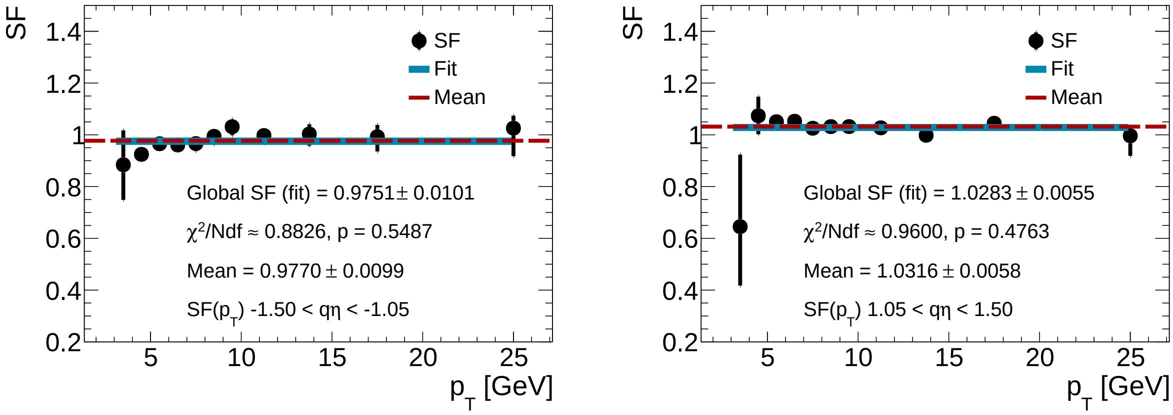

(a) -1.5 $< q\eta <$ -1.05 (b) 1.05 $\leq q\eta <$ 1.5

Figure 38: Trigger efficiency SFs as a function of p_T - endcap region

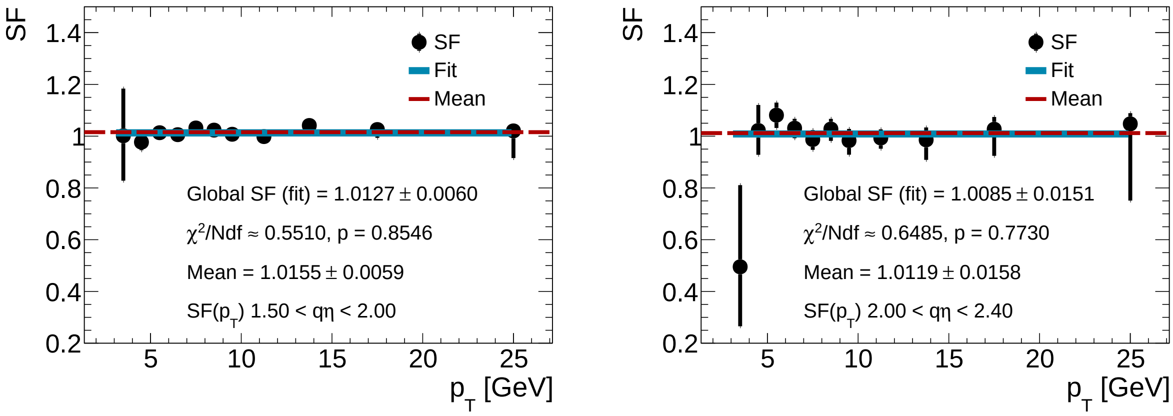

(a) 1.5 $< q\eta <$ 2 (b) 2 $\leq q\eta <$ 2.4

Figure 39: Trigger efficiency SFs as a function of p_T - endcap region

5.2 Systematic uncertainties

In every High Energy Physics (HEP) experiment, the uncertainties play a significant role in the final result of the analysis. Every previous figure contains only the statistical uncertainty, which depends solely on the entries in the bin. Systematic uncertainties allow us to verify the quality of the chosen analytical methodology and do not vanish even with high statistics. To estimate the systematics, an arbitrary choice of several sources of uncertainties is made:

- The $|d_0| < 1.1\,\text{mm}$ is replaced by the $|d_0|/\sigma_{d_0} < 3$, i.e. the transverse impact parameter significance, which corresponds to the number of standard deviations.
- Instead of the inclusive ZDC category, the dataset must pass the 0n0n selection (ZDC is not simulated in MC; it is assumed that MC does not have any background contribution)
- The "tag" muon has to pass the `muon_is_Medium` working point criteria instead of `muon_is_Tight`
- The primary condition for trigger matching $\Delta R < 0.3$ is changed to $\Delta R_{up} < 0.35$ and $\Delta R_{down} < 0.25$ (two-sided systematics)

The analysis is repeated for each variation independently, and a new set of SFs (SF_j) is generated. The systematic uncertainty is calculated using the formula below

$$\delta_{syst}^{i} = \sqrt{\sum_{j=0}^{n} |SF_{nominal} - SF_j|^2}, \tag{18}$$

where δ_{syst}^{i} is the systematic uncertainty in the i-th bin of p_T for a specific $q\eta$ interval, $SF_{nominal}$ is a value of SF that stems from the nominal selection (Section 3.2), and SF_j is the SF measured for the j-th systematic source. In the case of ΔR, only the larger systematic uncertainty component is included to δ_{syst}^{i}.

Figure 40 illustrates the SFs with individual systematic variations in the interval $-1.5 < q\eta < -1.05$, whereas Figure 41 shows only the nominal SF with their systematic uncertainties.

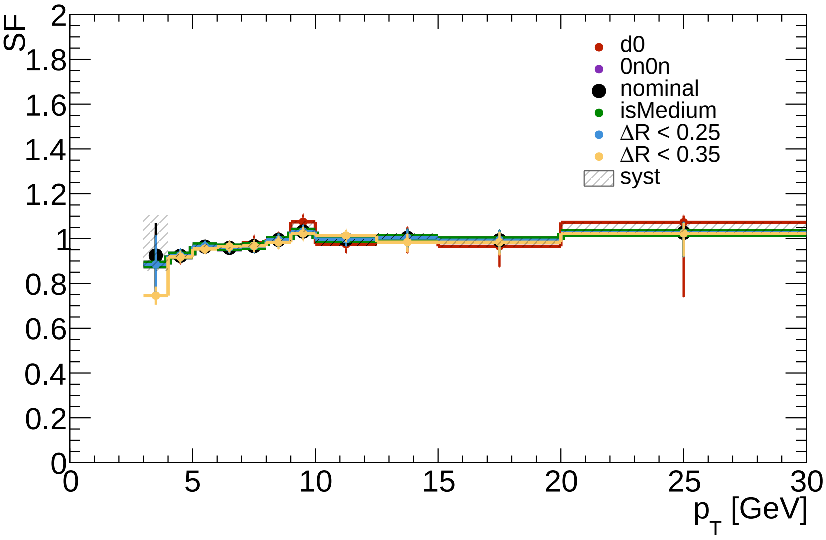

Figure 40: Trigger efficiency SFs with the systematic uncertainties and their sources - endcap region, $-1.5 < q\eta < -1.05$

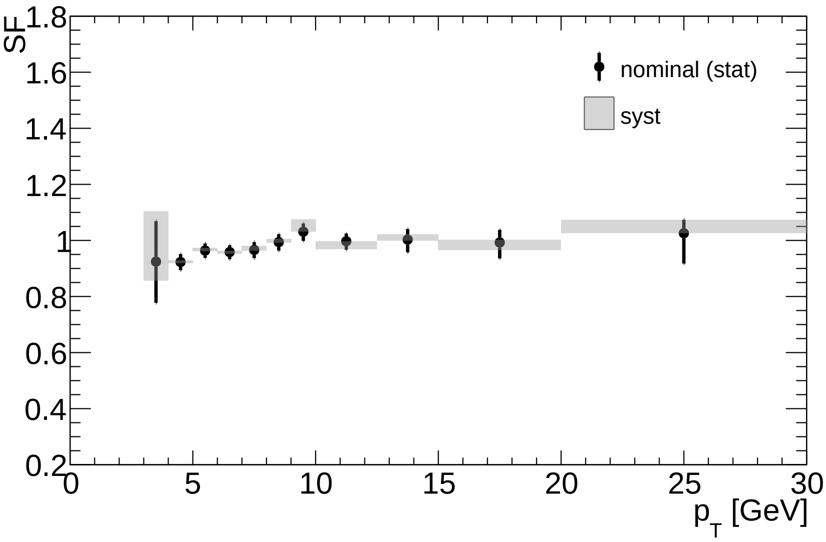

Figure 41: Trigger efficiency SFs with the systematic and statistical uncertainties as a function of p_T - endcap region, $-1.5 < q\eta < -1.05$

The discrepancies are most likely observed in the barrel region rather than in the endcap region. The remaining figures for other $q\eta$ bins are provided in the Appendix (Figures 63-68).

The differences between each systematic source are included in the Appendix (Figures 69-72). The most dominant systematic source originates from the ZDC category 0n0n requirement.

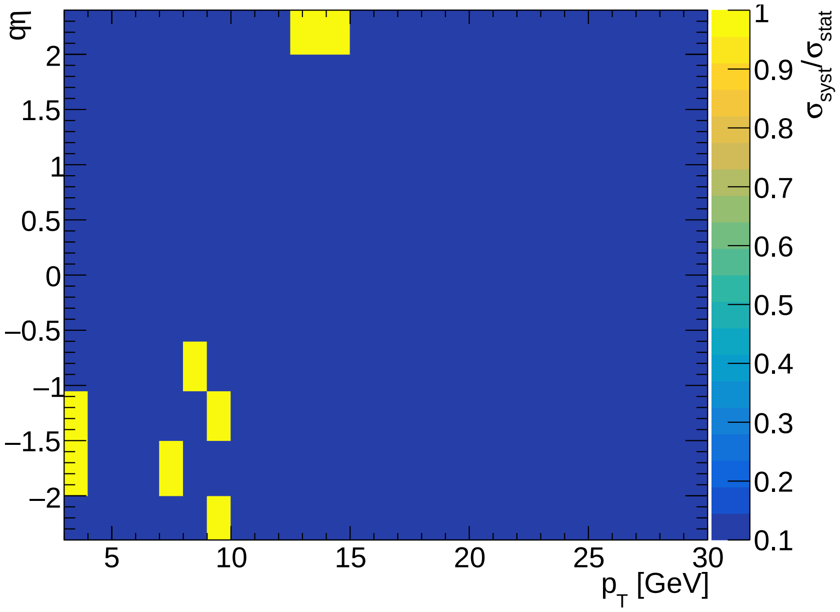

Figure 42: The dominance map in each $(p_T, q\eta)$ bin, indicating which uncertainty upper systematic/statistical dominates in each bin. Yellow - $\sigma_{syst} > \sigma_{stat}$, blue - $\sigma_{syst} < \sigma_{stat}$

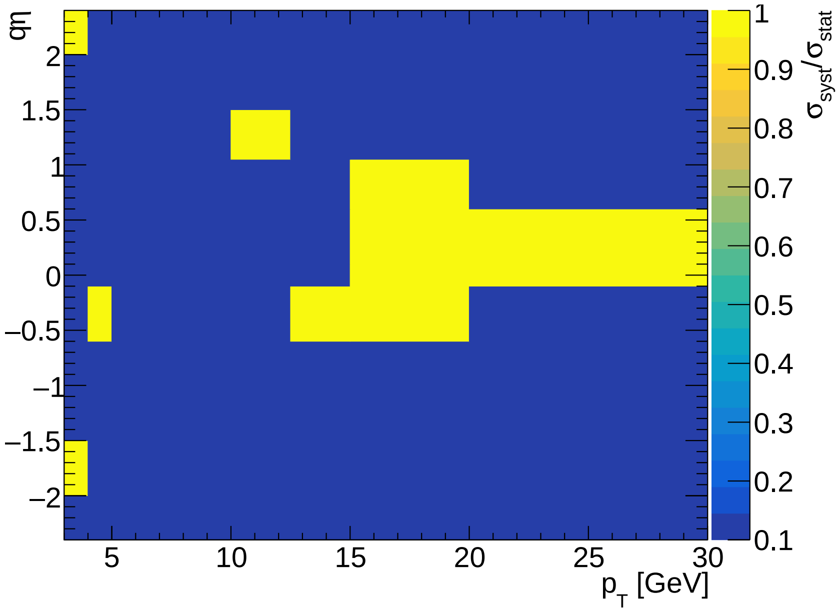

Figure 43: The dominance map in each $(p_T, q\eta)$ bin, indicating which uncertainty lower systematic/statistical dominates in each bin. Yellow - $\sigma_{syst} > \sigma_{stat}$, blue - $\sigma_{syst} < \sigma_{stat}$

Figures 42-43 provide evidence that the statistical uncertainties dominate over the systematic uncertainties. For better insight into which uncertainty dominates, the ratio is encoded as:

$$r = \begin{cases} 1.0, & \text{if } r > 1.0, \\ 0., & \text{if } r \leq 1.0. \end{cases} \tag{19}$$

It leads to the conclusion that the precision of the results is limited only by the number of entries; the full MC production is required for results with better precision.

6 Data acquisition in 2025

At the end of 2025, the ATLAS experiment collected Pb+Pb collisions at $\sqrt{s_{NN}} = 5.36\,\text{TeV}$, with data taking lasting for 21 days. To validate the quality of muons recorded in the UPC stream, the dataset from 2023 was used as a reference and compared with the 2025 data. The event selection is similar to that described in Section 3.2. The partial integrated luminosity for the analysed 2025 dataset is equal to $L_{int}^{2025} = 0.9841\,\text{nb}^{-1}$; for comparison, the 2025 data is normalised to the luminosity from 2023 $L_{int}^{2023} = 1.63\,\text{nb}^{-1}$.

6.1 Event selection

	Number of events	
Cut	2023	2025
All events	428811	1489893
At least one muon	414100	107962
~~passed GRL~~	~~414100~~	107962
Passed trigger	401566	107962
Exactly 2 muons with $p_T > 3\,\text{GeV}$ and $\|\eta\| < 2.5$	129551	79306
~~LowPt or~~ Loose identification criteria	115847	66776
Opposite charges	115345	66506
$A_{\phi}^{\mu,\mu} < 0.01$	102727	59165
$\|d_0\| < 1.1\,\text{mm}$	102563	59105

Table 3: The selection criteria taken from the analysis of 2023 data. Selection for 2025 data validation slightly differs from that described in Section 3.2

The GRL requirement is not applied to the 2025 dataset since the GRL is prepared only after the data-taking period is complete. Over the period from 2023 to 2025, several changes were made, such as the upgrade of the ATLAS L1 Topological Processor (L1Topo), named Phase-1. The HLT_mu3_L1MU3V_VTE50 trigger was replaced with HLT_mu3_L1MU3V_VjTE50; in addition, the working point of `muon_is_LowPt` was modified, so it was removed from the selection.

6.2 Comparison between 2023 and 2025 data

Figure 44 shows the η distributions and the overall comparison between the 2025 and 2023 data samples. In general, the distributions have similar shapes. However, the 2025 data reveal an excess over the 2023 data in the bins around ~ 1.4 for η^- and ~ -1.4 for η^+.

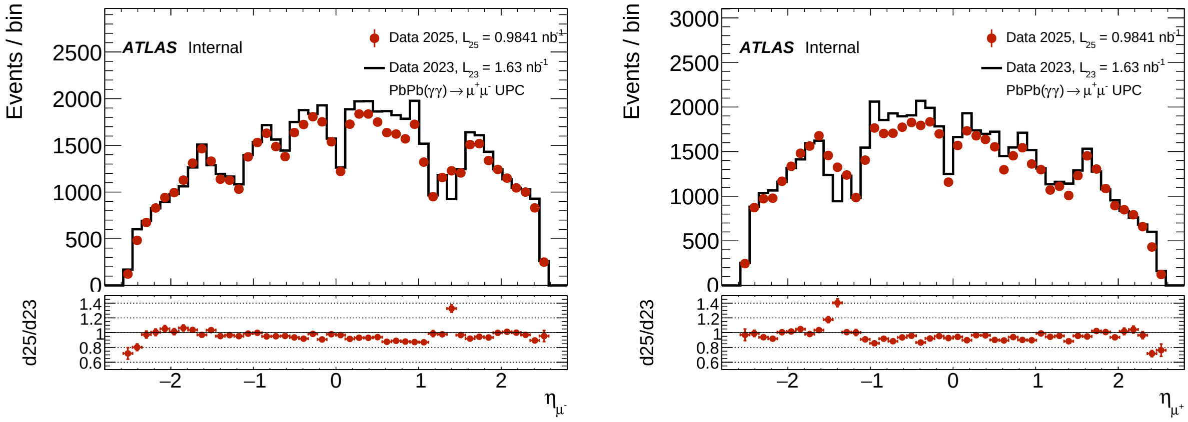

(a) Negatively charged (b) Positively charged

Figure 44: Pseudorapidity distributions of the positively and negatively charged muons

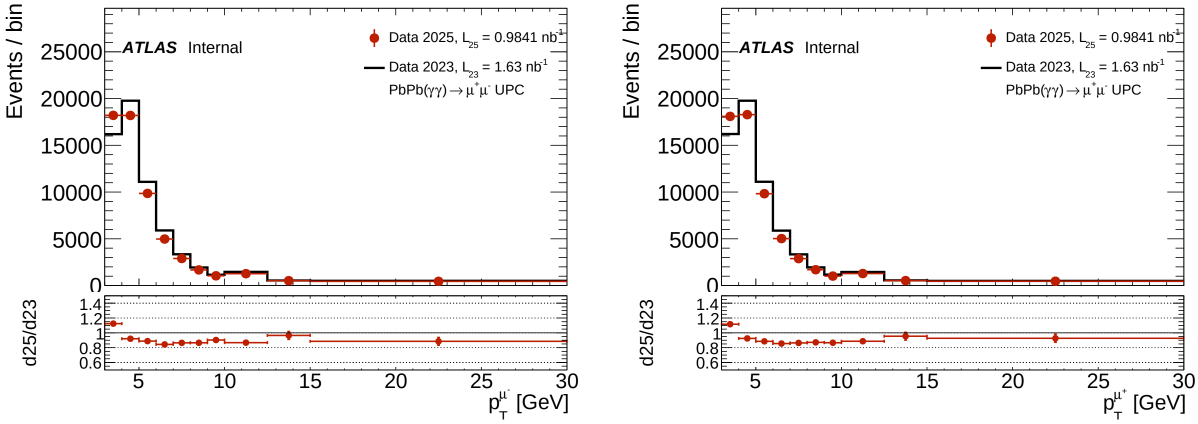

(a) Negatively charged (b) Positively charged

Figure 45: Transverse momentum distribution of the positively and negatively charged muon

The excess of the 2025 data over the 2023 data may be observed in Figure 45 in the first bin. The remaining part of the plot illustrates that the 2025 data are systematically lower up to $\sim 20\%$ than the 2023 data. At this stage of the analysis, it is hard to explain the diversity in the first bin.

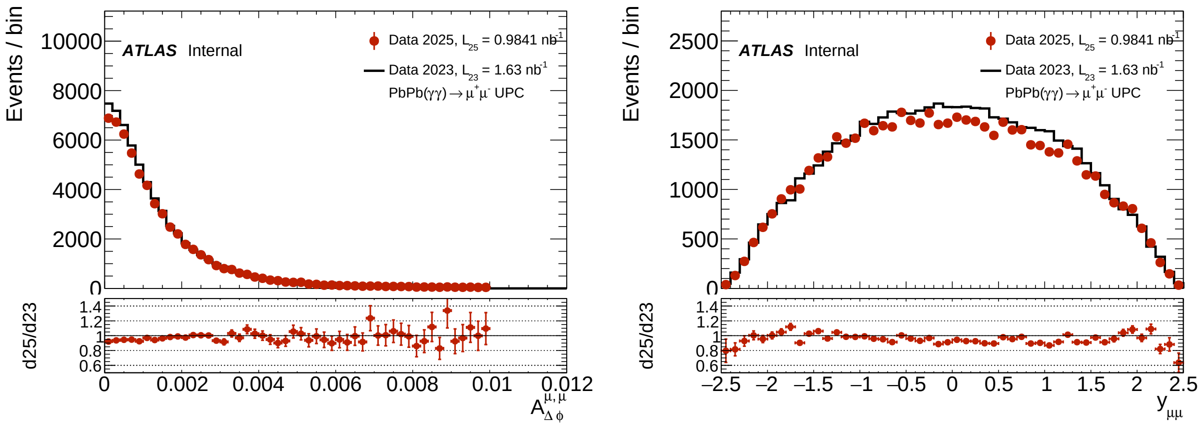

Figure 46: (left) Acoplanarity distribution, (right) rapidity distribution

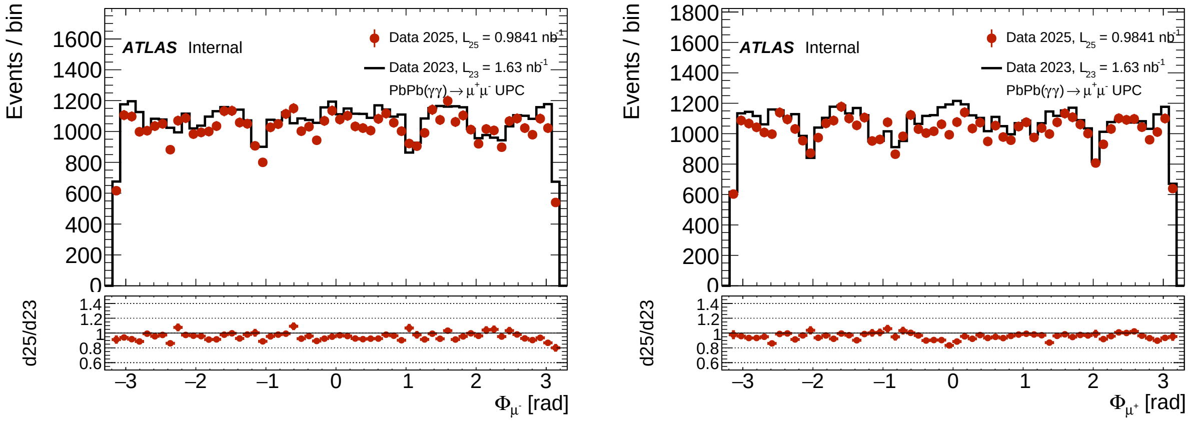

(a) Negatively charged (b) Positively charged

Figure 47: Azimuthal angle distribution of the positively and negatively charged muons

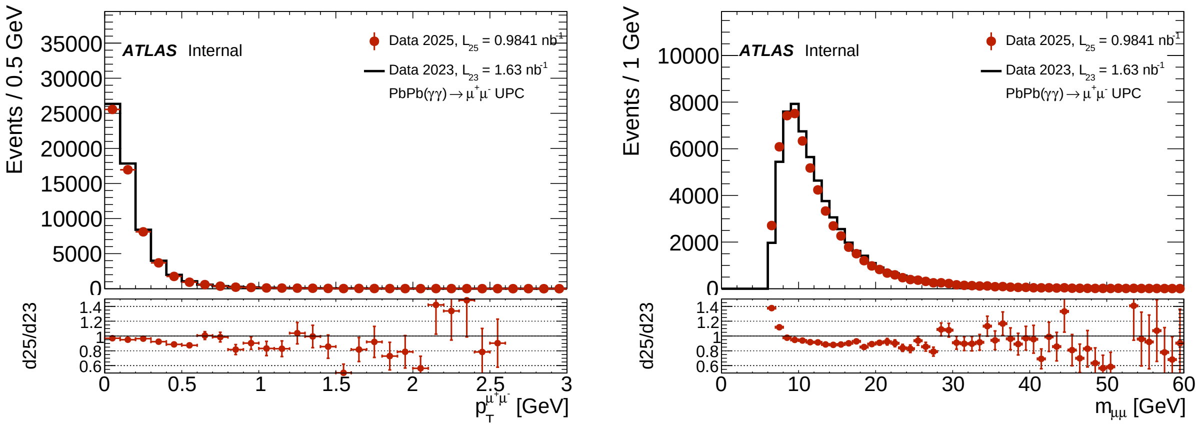

Figure 48: On the left panel - transverse momentum of muon pair distribution. On the right panel - invariant mass of dimuon system distribution

Figures 44-48 illustrate the comparison between the 2023 and 2025 data. The preliminary analysis shows two differences that should be studied further in future analyzes of UPC muons: (i) an overall normalisation of up to 20% between 2025 and 2023, and (ii) an excess of the 2025 data over the 2023 data at low-p_T and $m_{\mu\mu}$. It is also worth mentioning that at the beginning of the 2025 data-taking, the luminosity uncertainty is larger, up to the 15%.

6.3 The trigger efficiency results

Figures 49-50 represent the trigger efficiency results in the full p_T and $q\eta$ spectrum. The binning slightly differs to the binning in Section 4.2. The last two bins are merged into the single bin 15-30 GeV to balance the statistical uncertainties for the 2025 data. The methodology used to compute the trigger efficiency is the same as that described in Section 4.1 (the tag-and-probe method).

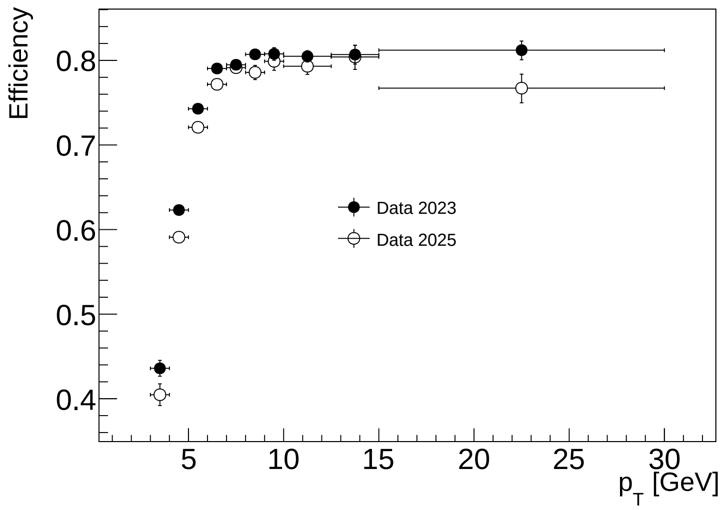

Figure 49: Trigger efficiency as a function of p_T in the full $q\eta$ spectrum. In 2023 data (full points) and 2025 data (open circles). Error bars represent statistical uncertainties

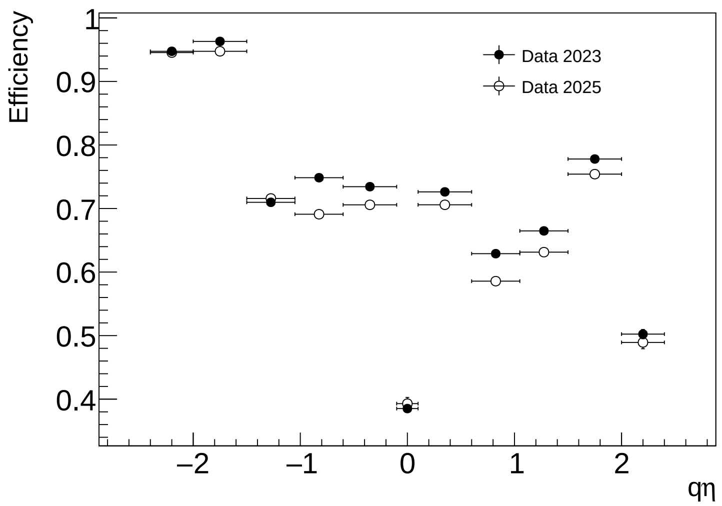

Figure 50: Trigger efficiency as a function of $q\eta$ in the full p_T spectrum. In 2023 data (full points) and 2025 data (open circles). Error bars represent statistical uncertainties

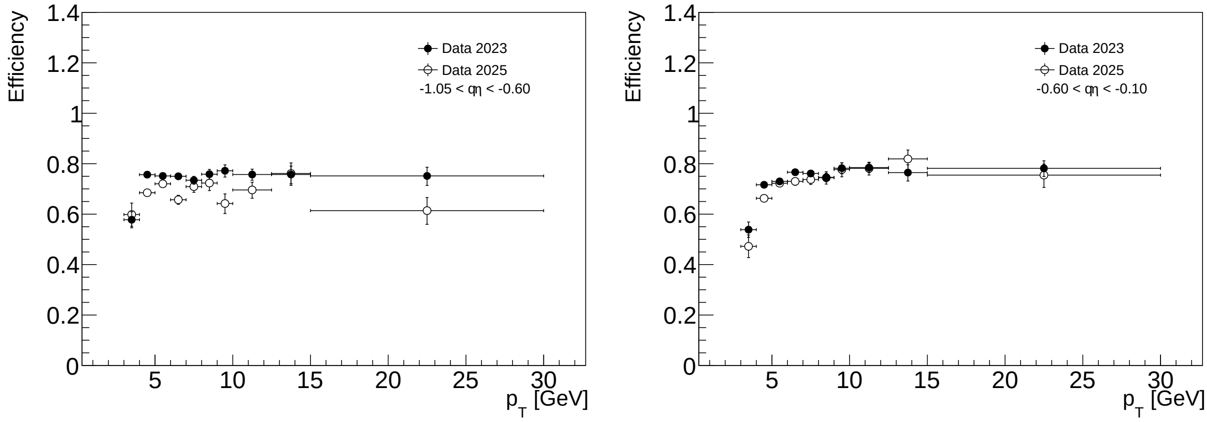

(a) -1.05 $< q\eta <$ -0.6

(b) -0.6 $\leq q\eta <$ -0.1

Figure 51: Trigger efficiency as a function of p_T - barrel region in 2023 data (full points) and 2025 data (open circles). Error bars represent statistical uncertainties

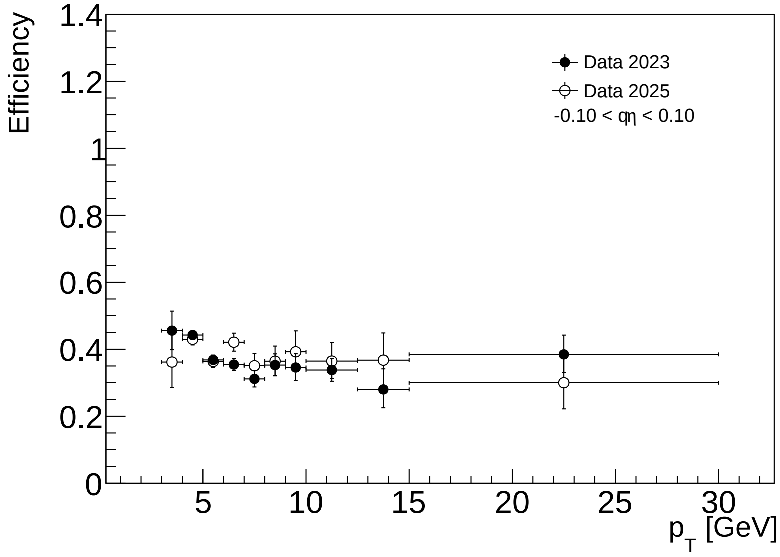

Figure 52: Trigger efficiency in the central region of barrel, -0.1 $< q\eta <$ 0.1, in 2023 data (full points) and 2025 data (open circles). Error bars represent statistical uncertainties

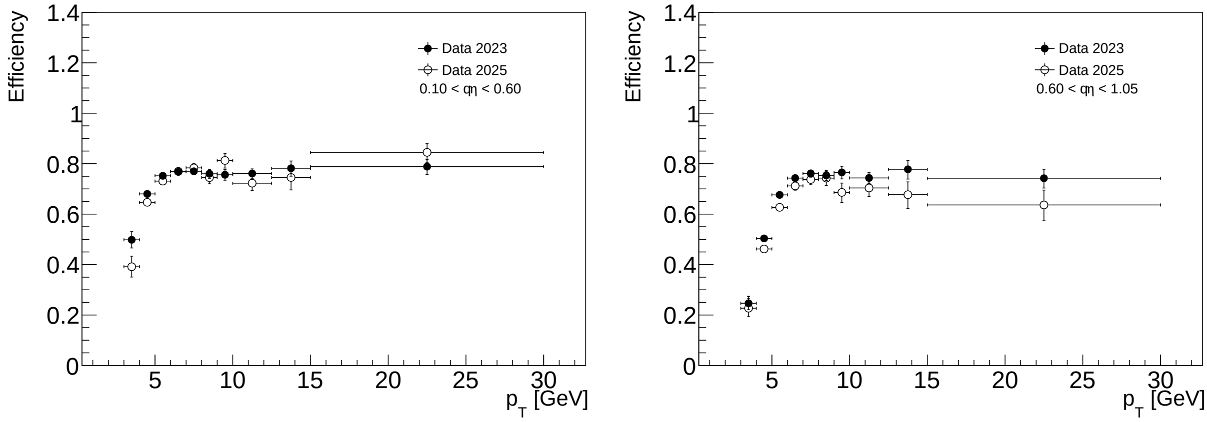

(a) $0.1 < q\eta < 0.6$ (b) $0.6 \leq q\eta < 1.05$

Figure 53: Trigger efficiency as a function of p_T - barrel region in 2023 data (full points) and 2025 data (open circles). Error bars represent statistical uncertainties

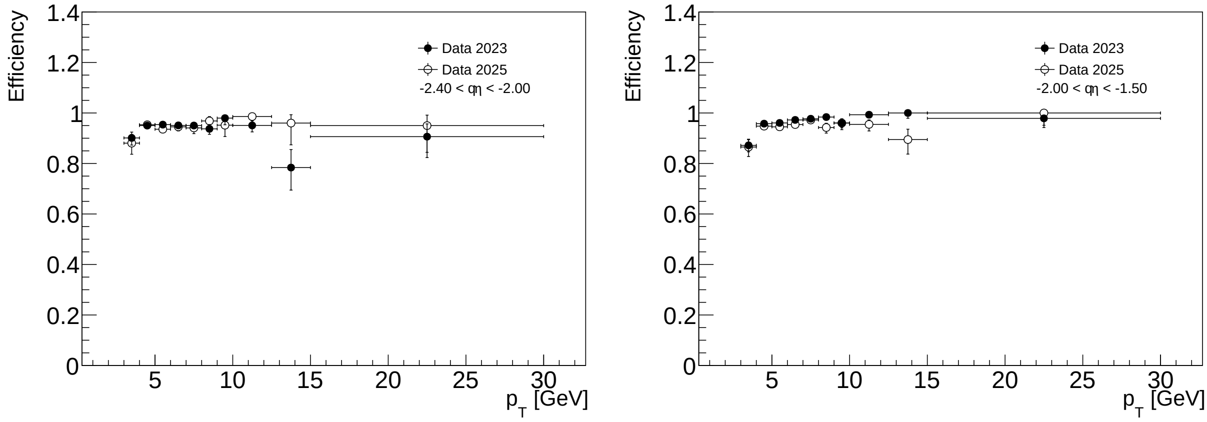

(a) $-2.4 < q\eta < -2$ (b) $-2 \leq q\eta < -1.5$

Figure 54: Trigger efficiency as a function of p_T - endcap region in 2023 data (full points) and 2025 data (open circles). Error bars represent statistical uncertainties

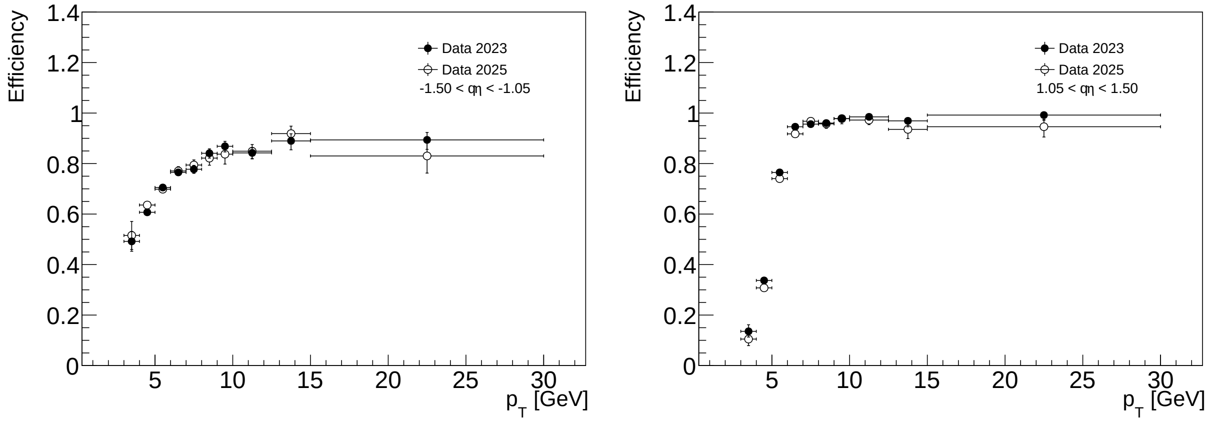

(a) $-1.5 < q\eta < -1.05$ (b) $1.05 \leq q\eta < 1.5$

Figure 55: Trigger efficiency as a function of p_T - endcap region in 2023 data (full points) and 2025 data (open circles). Error bars represent statistical uncertainties

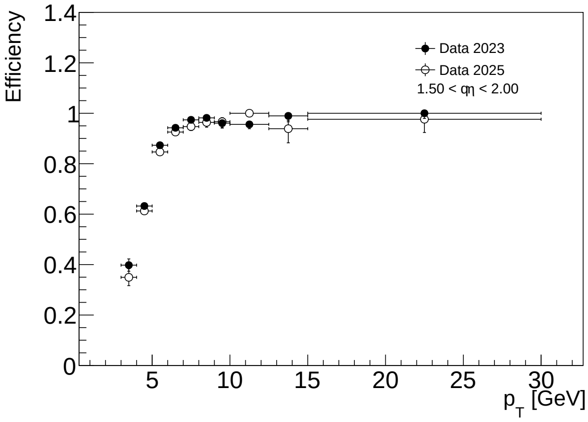

(a) $1.5 < q\eta < 2$

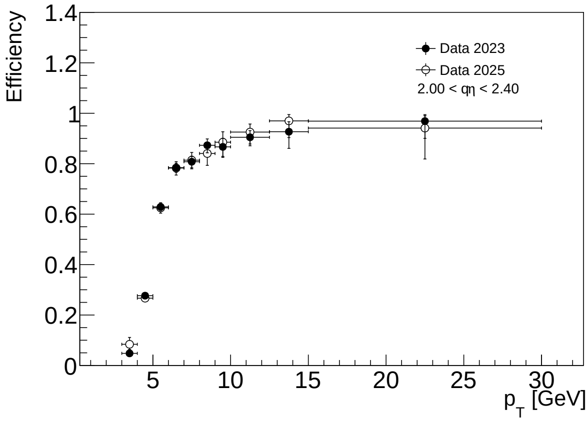

(b) $2 \leq q\eta < 2.4$

Figure 56: Trigger efficiency as a function of p_T - endcap region in 2023 data (full points) and 2025 data (open circles). Error bars represent statistical uncertainties

The trigger efficiencies in the barrel region are shown in Figures 51-53. Overall, the trigger efficiencies in 2025 are lower than those measured in 2023. The origin of this discrepancy, at the current stage of the analysis, is not yet understood. On the other hand, in the endcap region (Figures 54-56), a better agreement between the two datasets can be observed. At the low-p_T, the 2025 data are slightly lower than the 2023 data.

7 Conclusions

This thesis presents a study of the `L1_MU3V_VTE50` muon trigger efficiency using the Run 3 Pb+Pb data collected at $\sqrt{s_{NN}} = 5.36\,\text{TeV}$ in 2023. The dataset originates from the UPC stream, where the hadronic background is strongly suppressed, and the interactions are dominated by electromagnetic photon exchange.

To distinguish the signal process of exclusive dimuon $\gamma\gamma \to \mu^-\mu^+$ production, a dedicated dimuon selection is applied for both data and MC simulation. All events are required to pass the trigger requirement and contain exactly two reconstructed muons with opposite charges. The transverse momentum of each muon must be greater than 3 GeV, and the absolute value of the muon pseudorapidity must be less than 2.5. The dimuon acoplanarity is set to be less than 0.01, which is compatible with the back-to-back topology. Last but not least, the vertexing requirement on the transverse impact parameter is applied: $|d_0| < 1.1\,\text{mm}$ for each reconstructed muon track. After the event selection, 102823 data events are retained and 44789 in MC simulation. Control plots in the data are compared to the MC simulation generated with SuperChic interfaced with Pythia8 for the $\gamma\gamma \to \mu^-\mu^+$ process. Validation samples with 50 000 events for the dimuon production are used for three mass slices. In general, a good agreement is found. Although there are a few mismatches, they do not affect the trigger efficiency results. The main issue to be investigated before launching the full MC production is the shape difference in the $|\mathbf{p}_T^{\mu\mu}|$ distribution. The predicted number of MC events for the full MC production is 1.4×10^7 in the $m_{\mu\mu} \in [4, 7]$ GeV, 4×10^6 in the $m_{\mu\mu} \in [7, 20]$ GeV, 1.5×10^5 for $m_{\mu\mu} > 20\,\text{GeV}$. The comparison between the old MC samples (0n0n ZDC category) and the new MC samples (inclusive ZDC category) is also presented. The old MC samples were inadvertently produced in the 0n0n category, and are not used in the nominal analysis; fixing this problem was crucial to obtain a good agreement in control plots of muon p_T and mass of the dimuon system.

Furthermore, the tag-and-probe method is applied for data and MC simulation to measure the L1_MU3V trigger efficiency. The $\Delta R(\mu_{reco}, \mu_{L1}) < 0.3$ requirement is chosen as a trigger matching criterion. The trigger efficiencies are measured as a function of p_T or $q\eta$ and are divided into two regions: the barrel region ($|q\eta| < 1.05$) and the endcap region ($|q\eta| > 1.05$). In data (MC), the trigger efficiency in the barrel region is, on average, about 0.8 (0.9). In the endcap region, the data and MC are more consistent with each other, but they are strongly asymmetric around zero because of the toroidal magnetic field. For muons with $p_T > 7\,\text{GeV}$, the trigger efficiency is symmetric in $q\eta$ and ranges from 0.78 to 1.00.

To quantify differences between trigger efficiencies in the data and MC simulation, the SFs are measured in the barrel and endcap regions. The SF values in the barrel region are found to be in the range of 0.8-0.9, and 0.95-1.05 in the endcap region. The constant-function fit in muon p_T provides a good description of the SF values. There are two important conclusions that stem from that: (i) the SF values show no dependence on p_T, (ii) the differences between efficiencies in data and MC simulation are significant.

The statistical uncertainties of the efficiencies are estimated using the Clopper-Pearson method and are, therefore, asymmetric. The upper and lower statistical uncertainties for SFs are propagated separately. In addition, the systematic uncertainties from a few sources are evaluated; the leading systematic source originates from the ZDC 0n0n category. In general, the systematic uncertainties are lower than the statistical uncertainties; therefore, the current measurement is statistically limited. It can be improved in the future by increasing a number of produced simulates events.

The preliminary analysis of the early 2025 Pb+Pb data collected by the ATLAS experiment at $\sqrt{s_{\text{NN}}} = 5.36\,\text{TeV}$ is also performed. The data sample corresponds to an initial subset of the 2025 dataset, with an integrated luminosity of $L_{int}^{2025} = 0.9841\,\text{nb}^{-1}$. To verify the quality of the 2025 data, a comparison with the 2023 data analysed in this thesis is made. In general, control plots for the 2025 and 2023 data show reasonable agreement, but some identified discrepancies need further investigation. The identified deviations from the 2023 reference data may be due to: (i) several changes in the detector which were introduced between 2023 and 2025 runs, (ii) the fact that the 2025 dataset used events without GRL selection, and (iii) online luminosity calibration is applied, which carries an uncertainty up to 15%.

References

[1] G. Aad, T. Abajyan, B. Abbott, and et al. Observation of a new particle in the search for the standard model higgs boson with the atlas detector at the lhc. *Physics Letters B*, 716(1):129, sep 2012.

[2] G. Aad, T. Abajyan, B. Abbott, and et al. Evidence for light-by-light scattering in heavy-ion collisions with the atlas detector at the lhc. *Nature Physics*, 13(9):852–858, August 2017.

[3] M. Aaboud, G. Aad, B. Abbott, and et al. Observation of higgs boson production in association with a top quark pair at the lhc with the atlas detector. *Physics Letters B*, 784:173–191, sep 2018.

[4] Riccardo Maria Bianchi and ATLAS Collaboration. ATLAS experiment schematic or layout illustration. General Photo, 2022.

[5] Joao Pequenao. Computer generated image of the ATLAS inner detector. 2008.

[6] Joao Pequenao. Computer Generated image of the ATLAS calorimeter. 2008.

[7] Joao Pequenao. Computer generated image of the ATLAS Muons subsystem. 2008.

[8] T Kawamoto, S Vlachos, L Pontecorvo, J Dubbert, G Mikenberg, P Iengo, C Dallapiccola, C Amelung, L Levinson, R Richter, and D Lellouch. New Small Wheel Technical Design Report. Technical report, 2013. ATLAS New Small Wheel Technical Design Report.

[9] Ana Maria Rodriguez Vera and Joao Antunes Pequenao. ATLAS Detector Magnet System. General Photo, 2021.

[10] Izaak Neutelings. Cms coordinate system. `https://tikz.net/axis3d_cms/`, 2017.

[11] Izaak Neutelings. Pseudorapidity. `https://tikz.net/axis2d_pseudorapidity/`, 2017.

[12] C. F. von Weizsaecker. Zur theorie der kernstruktur. *Zeitschrift für Physik*, 88(7-8):612–626, 1934.

[13] E. J. Williams. Nature of the high energy particles of penetrating radiation and status of ionization and radiation formulae. *Phys. Rev.*, 45:729–730, May 1934.

[14] E. Fermi. Über die wahrscheinlichkeit der wirkung von atomen in der quantenmechanik. *Zeitschrift für Physik*, 29(1):315–327, 1924.

[15] Izaak Neutelings. Pb-pb collision with impact parameter. `https://tikz.net/pbpb_collisions/`, 2024.

[16] Carlos A. Bertulani, Spencer R. Klein, and Joakim Nystrand. Physics of ultra-peripheral nuclear collisions. *Annual Review of Nuclear and Particle Science*, 55(1):271–310, December 2005.

[17] G. N. Watson. *A Treatise on the Theory of Bessel Functions*. Cambridge University Press, Cambridge, 2 edition, 1944.

[18] Gerhard Baur, Kai Hencken, and Dirk Trautmann. Photon-photon physics in very peripheral collisions of relativistic heavy ions. *Journal of Physics G: Nuclear and Particle Physics*, 24(9):1657–1691, September 1998.

[19] Georges Aad et al. Exclusive dimuon production in ultraperipheral pbpb collisions at snn 5.02 tev with atlas. *Phys. Rev. C*, 104:024906, 2021.

[20] L. A. Harland-Lang, V. A. Khoze, and M. G. Ryskin. Exclusive LHC physics with heavy ions: SuperChic 3. *Eur. Phys. J. C*, 79(1):39, 2019.

[21] Agnieszka Ewa Ogrodnik. Exclusive dilepton production in ultraperipheral Pb+Pb collisions in ATLAS. Technical report, CERN, Geneva, 2023.

[22] M Rybar. Triggering on jets in heavy ion collisions at the ATLAS experiment. Technical report, CERN, Geneva, 2009. 31.3.2009.

[23] G. Aad et al. Performance of the atlas muon triggers in run 2. *Journal of Instrumentation*, 15(09):P09015–P09015, September 2020.

[24] Karolina Domijan. Exclusive production of opposite-charge muon pairs in ultra-peripheral heavy-ion collisions in the atlas experiment at the lhc. 2021.

List of Figures

Appendix

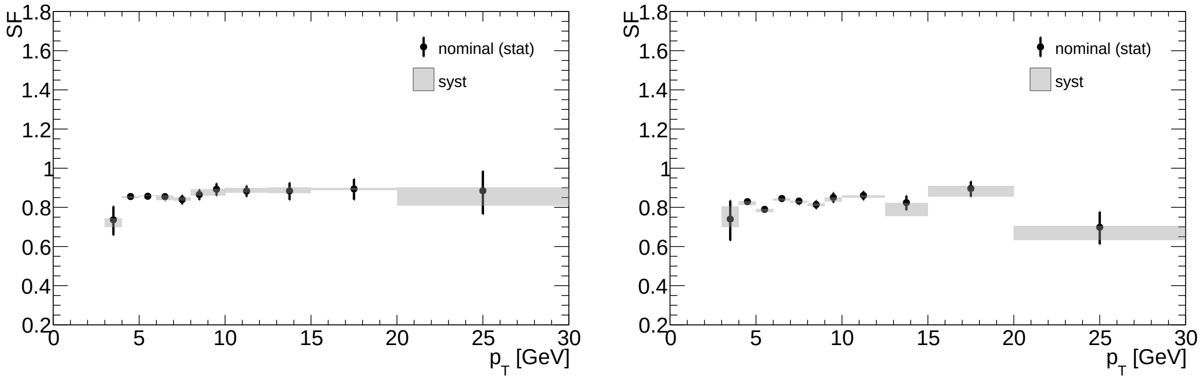

(a) -1.05 < $q\eta$ < -0.6 (b) -0.6 ≤ $q\eta$ < -0.1

Figure 57: Trigger efficiency SFs with the systematic and statistical uncertainties as a function of p_T - barrel region

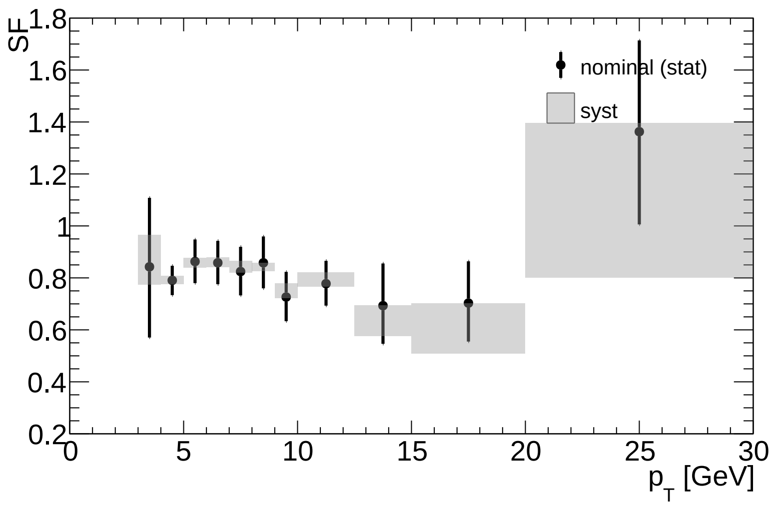

Figure 58: Trigger efficiency SFs with the systematic and statistical uncertainties as a function of p_T - barrel region, $-0.1 < q\eta < 0.1$

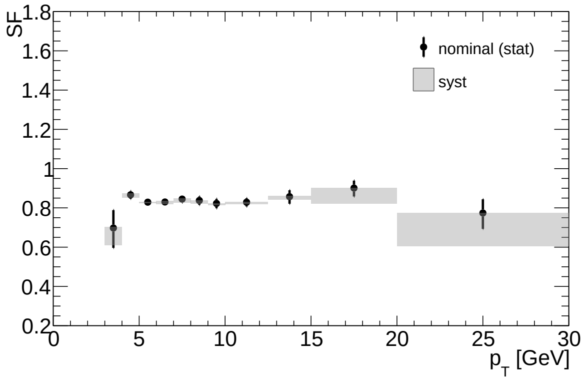

(a) $0.1 < q\eta < 0.6$

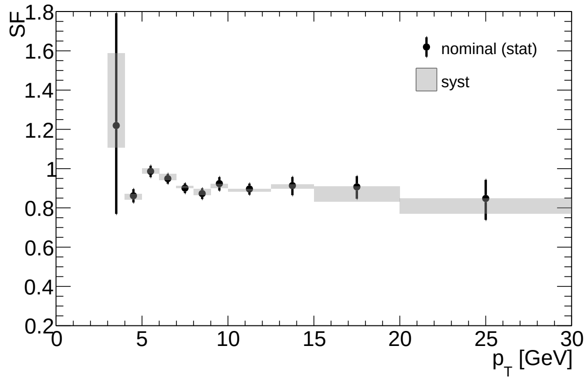

(b) $0.6 \leq q\eta < 1.05$

Figure 59: Trigger efficiency SFs with the systematic and statistical uncertainties as a function of p_T - barrel region

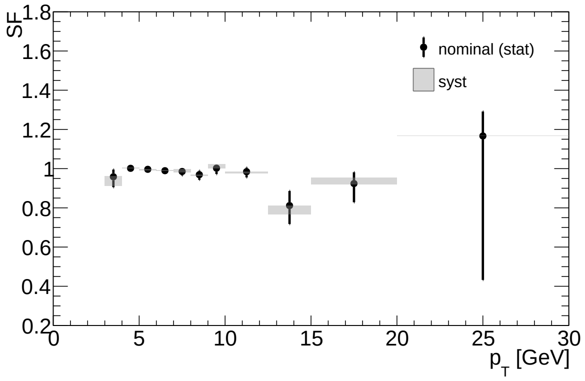

(a) $-2.4 < q\eta < -2$

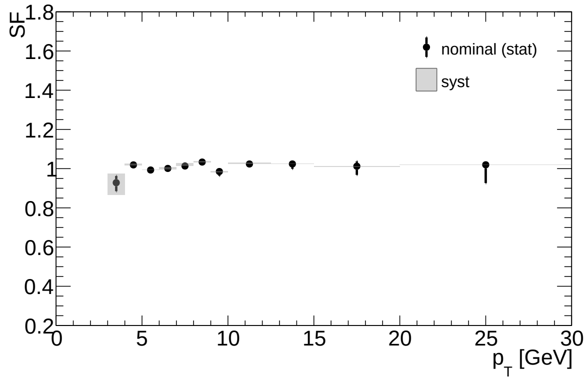

(b) $-2 \leq q\eta < -1.5$

Figure 60: Trigger efficiency SFs with the systematic and statistical uncertainties as a function of p_T - endcap region

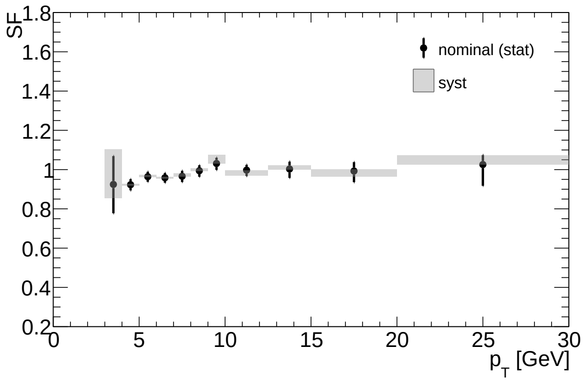

(a) $-1.5 < q\eta < -1.05$

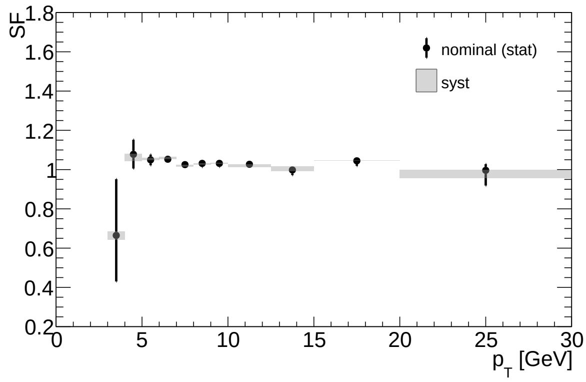

(b) $1.05 \leq q\eta < 1.5$

Figure 61: Trigger efficiency SFs with the systematic and statistical uncertainties as a function of p_T - endcap region

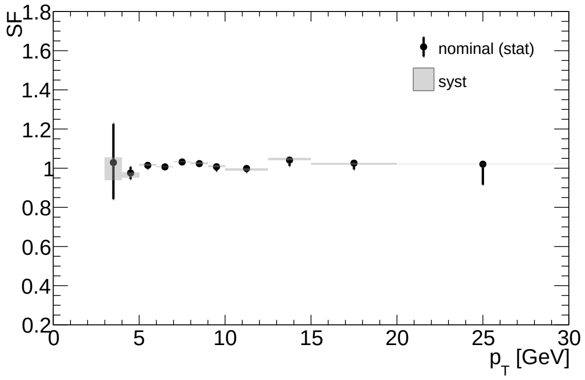

(a) $1.5 < q\eta < 2$

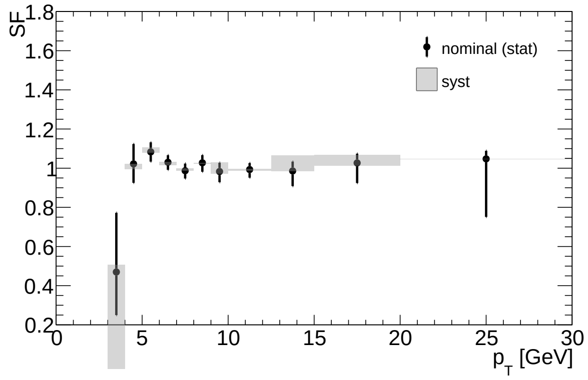

(b) $2 \leq q\eta < 2.4$

Figure 62: Trigger efficiency SFs with the systematic and statistical uncertainties as a function of p_T - endcap region

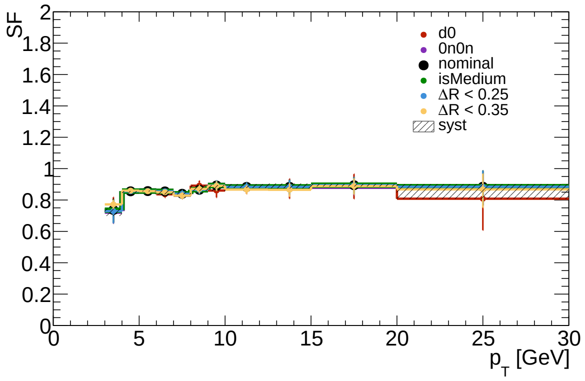

(a) -1.05 $< q\eta <$ -0.6

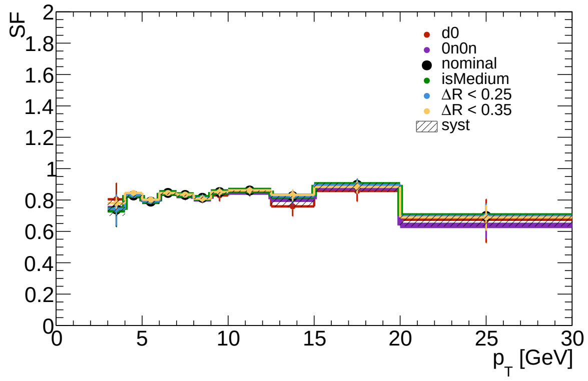

(b) -0.6 $\leq q\eta <$ -0.1

Figure 63: Trigger efficiency SFs with the systematic uncertainties and their sources - barrel region

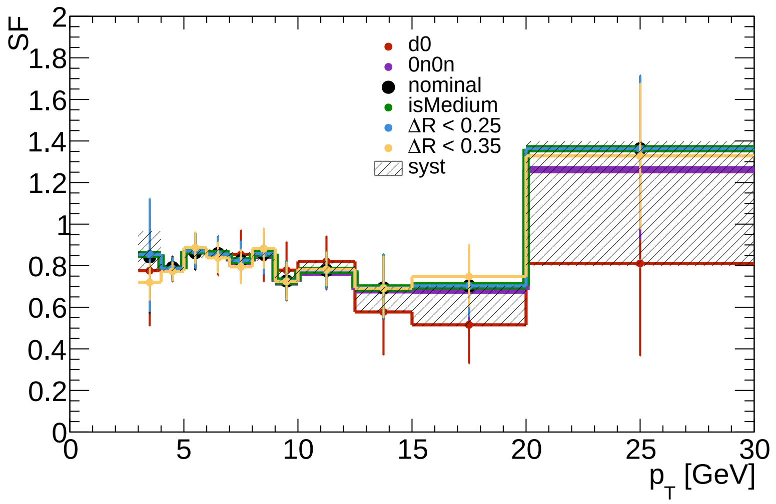

Figure 64: Trigger efficiency SFs with the systematic uncertainties and their sources - barrel region, $-0.1 < q\eta < 0.1$

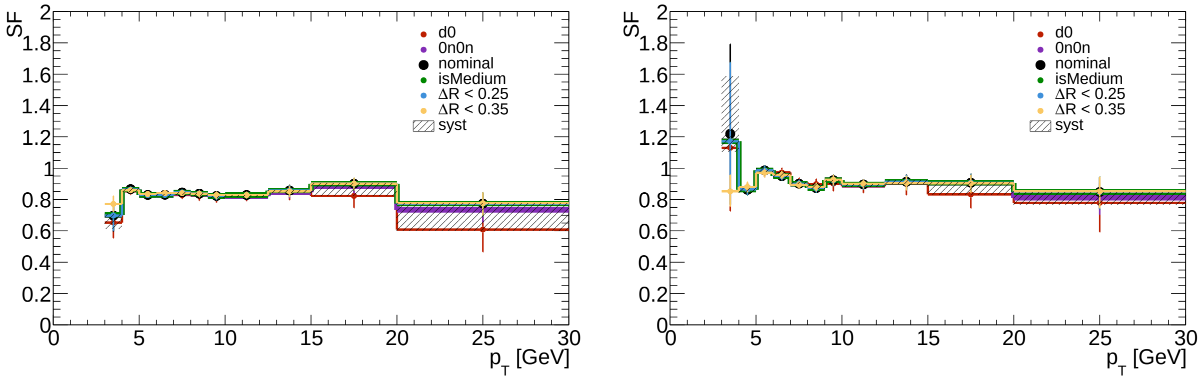

(a) $0.1 < q\eta < 0.6$ (b) $0.6 \leq q\eta < 1.05$

Figure 65: Trigger efficiency SFs with the systematic uncertainties and their sources - barrel region

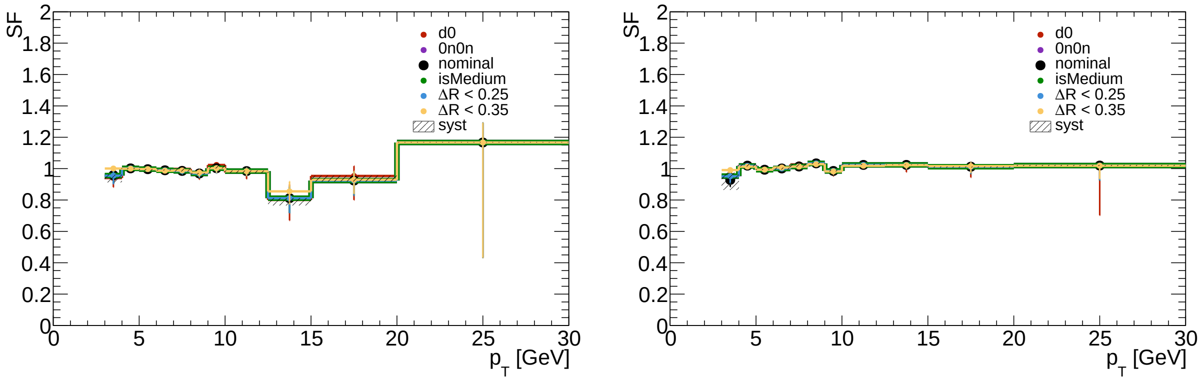

(a) $-2.4 < q\eta < -2$ (b) $-2 \leq q\eta < -1.5$

Figure 66: Trigger efficiency SFs with the systematic uncertainties and their sources - endcap region

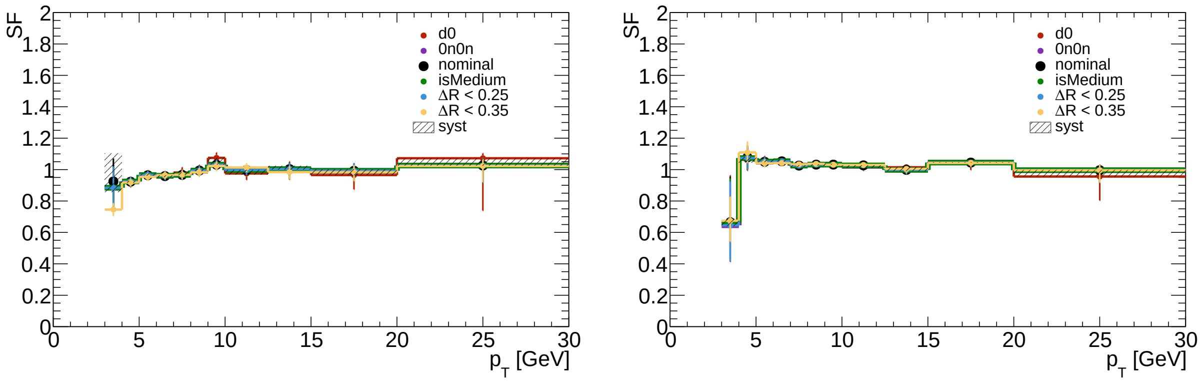

(a) $-1.5 < q\eta < -1.05$ (b) $1.05 \leq q\eta < 1.5$

Figure 67: Trigger efficiency SFs with the systematic uncertainties and their sources - endcap region

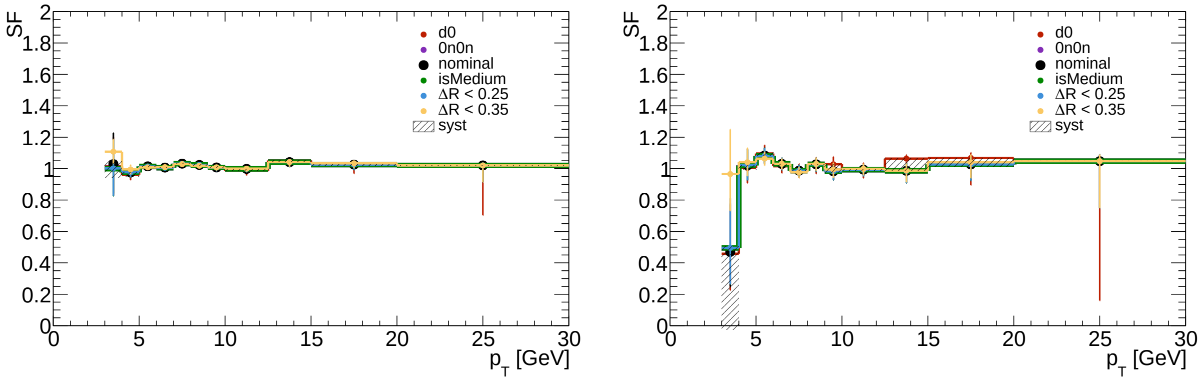

(a) $1.5 < q\eta < 2$ (b) $2 \leq q\eta < 2.4$

Figure 68: Trigger efficiency SFs with the systematic uncertainties and their sources - endcap region

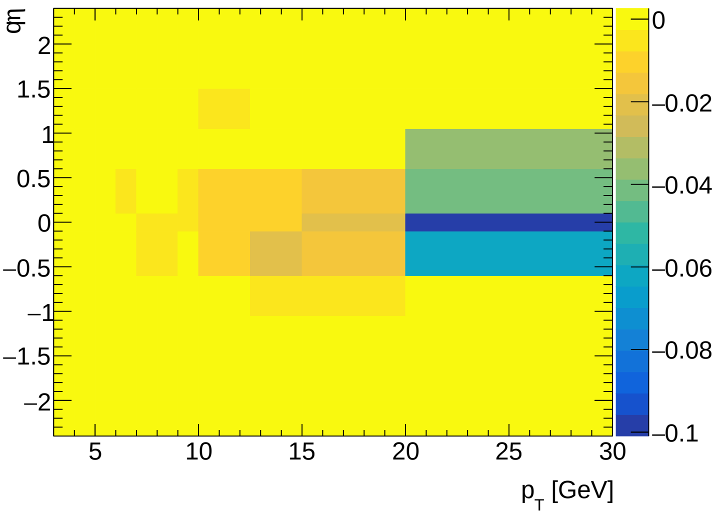

Figure 69: The SF difference map for the changed d_0 requirement

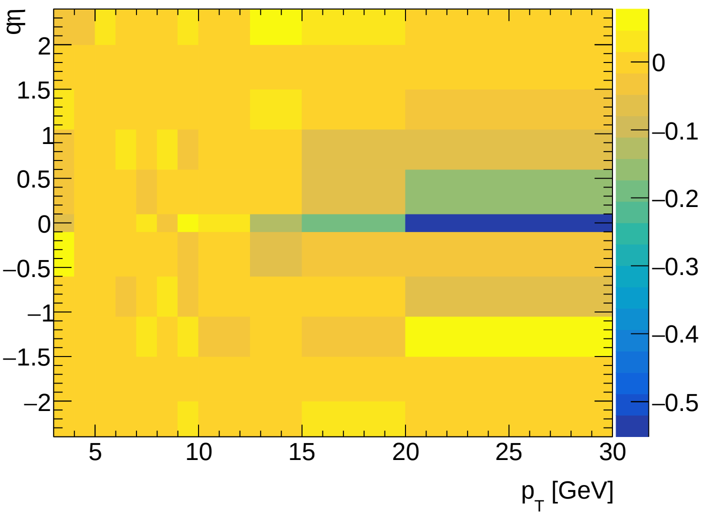

Figure 70: The SF difference map for the 0n0n category

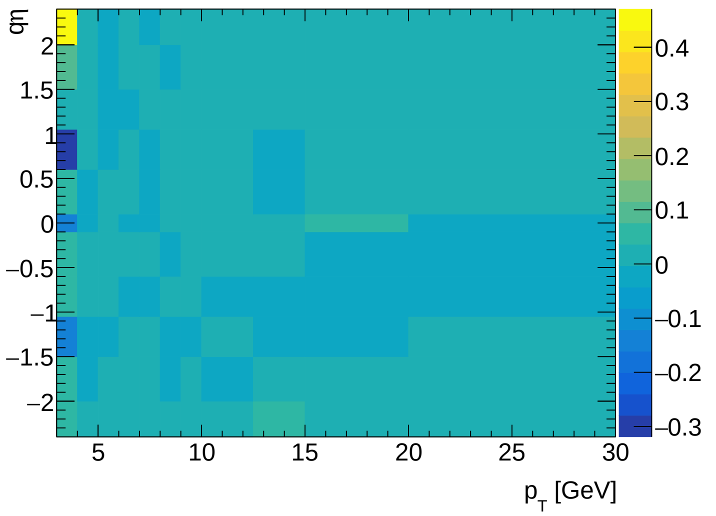

Figure 71: The SF difference map for the `muon_is_Medium` working point

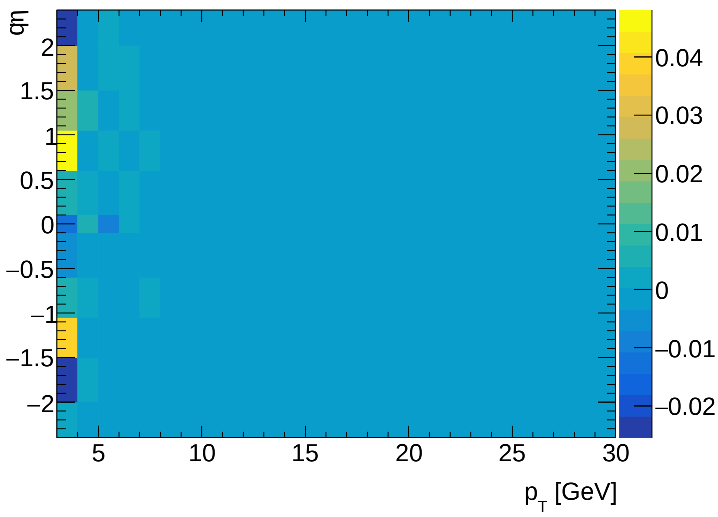

Figure 72: The SF difference map for the two-sided ΔR systematic source